

Strain budget of the Ecuador-Colombia subduction zone: a stochastic view

B. Gombert^{a,*}, Z. Duputel^a, R. Jolivet^b, M. Simons^c, J. Jiang^d, C. Liang^e, E. Fielding^e, L. Rivera^a

^a*Institut de Physique du Globe de Strasbourg, UMR7516, Université de Strasbourg, EOST/CNRS*

^b*Laboratoire de géologie, Département de Géosciences, École Normale Supérieure, PSL Research University, CNRS UMR 8538, Paris, France*

^c*Seismological Laboratory, Geological and Planetary Sciences, California Institute of Technology, Pasadena, California, USA*

^d*Institute of Geophysics and Planetary Physics, University of California, San Diego, La Jolla, California, USA*

^e*Jet Propulsion Laboratory, California Institute of Technology, Pasadena, California, USA*

Abstract

The 2016 Pedernales earthquake ($M_W=7.8$) ruptured a portion of the Colombia-Ecuador subduction interface where several large historical earthquakes have been documented since the great 1906 earthquake ($M=8.6$). Considering all significant ruptures that occurred in the region, it has been suggested that the cumulative moment generated co-seismically along this part of the subduction over the last century exceeds the moment deficit accumulated inter-seismically since 1906. Such an excess challenges simple models with earthquakes resetting the elastic strain accumulated inter-seismically in locked asperities. These inferences are however associated with large uncertainties that are generally unknown. The impact of spatial smoothing constraints on co-seismic and inter-seismic models also prevents any robust assessment of the strain budget. We propose a Bayesian kinematic slip model of the 2016 Pedernales earthquake using the most comprehensive dataset to date including InSAR and

*Corresponding author

Email address: gombert@unistra.fr (B. Gombert)

GPS offsets, tsunami waveforms, and kinematic records from high-rate GPS and strong-motions. In addition, we use inter-seismic geodetic velocities to produce a probabilistic inter-seismic coupling model of the subduction interface. Our stochastic co-seismic and inter-seismic solutions include the ensemble of all plausible models consistent with our prior information and that fit the observations within uncertainties. The analysis of these model ensembles indicates that an excess of co-seismic moment during the 1906 - 2016 period is likely in Central Ecuador only if we assume that 1942 and 2016 earthquakes are collocated. If this assumption is relaxed, we show that this conclusion no longer holds given uncertainties in co- and inter-seismic processes. The comparison of 1942 and 2016 teleseismic records reveals large uncertainties in the location of the 1942 event, hampering our ability to draw strong conclusions on the unbalanced moment budget in the region. Our results also show a heterogeneous coupling of the subduction interface that coincides with two slip asperities in our co-seismic model for the 2016 Pedernales earthquake and with the location of historical ruptures in 1958, 1979 and 1998. The spatial variability in coupling and complexity in earthquake history suggest strong heterogeneities in frictional properties of the subduction megathrust.

Keywords: Ecuador-Colombia subduction zone, Strain budget, Bayesian inversion, Kinematic source model, Geodetic coupling model

1. Introduction

A long standing question is the existence of persistent fault segments remaining locked in the inter-seismic period and failing suddenly during earthquakes while the surround-

4 ing interface creeps continuously. This conceptual model predicts so-called “characteristic”
5 earthquakes repeatedly rupturing the same locked fault segments with either periodic, time-
6 predictable or slip-predictable behaviours (Shimazaki and Nakata, 1980; Schwartz and Cop-
7 persmith, 1984). This paradigm is contradicted by an increasing number of observations
8 showing that the same fault area can break entirely in a single large earthquake ($M_W > 8.5$)
9 but also in a series of smaller ruptures. A remarkable example of such behaviour is the
10 Colombia-Ecuador subduction zone that experienced a complex sequence of earthquakes
11 since the beginning of the 20th century (see Figure 1). In 1906, the great $M_W = 8.6$ earth-
12 quake ruptured a ~ 500 -km-long segment of the subduction interface (Gutenberg and Richter,
13 1949; Ye et al., 2016). Several decades later, the same area was re-ruptured by a series of
14 smaller $M_W \leq 8.2$ events in 1942, 1958, 1979 and 1998 (Kanamori and McNally, 1982; Beck
15 and Ruff, 1984; Mendoza and Dewey, 1984; Chlieh et al., 2014). In April 2016, the region
16 in the vicinity of the 1942 Ecuador event was again ruptured by the $M_W = 7.8$ Pedernales
17 earthquake (Ye et al., 2016; He et al., 2017; Nocquet et al., 2017; Yi et al., 2018). Such vari-
18 ability among successive ruptures is also observed in other regions like Japan and Sumatra
19 where recent $M_W \sim 9$ megathrust earthquakes ruptured large fault segments that previously
20 experienced a serie of smaller events (Simons et al., 2011; Lay, 2015).

21 In addition to such spatial variability among successive ruptures, major earthquakes in
22 the Colombia-Ecuador subduction zone seem to be clustered in time. Specifically, it has been
23 recently suggested that the seismic moment of the 1942, 1958 and 1979 earthquakes exceeds
24 the deficit accumulated since 1906 and that the 2016 Pedernales event may be associated with

25 more fault slip than the deficit accumulated since the 1942 earthquake (Nocquet et al., 2017).
26 Similar observations are reported in other regions, for example in 1797 and 1833 earthquakes
27 in Sumatra (Sieh et al., 2008), 1812 and 1857 earthquakes in California (Jacoby et al., 1988;
28 Heaton, 1990), and for the 2003 $M_W=7.6$ and 2013 $M_W=7.8$ Scotia sea earthquakes (Vallée
29 and Satriano, 2014). Such spatial and temporal clustering can be caused by spatial variations
30 of fault coupling associated with heterogeneous frictional properties (Kaneko et al., 2010).
31 Moreover, there can be fluctuations in the patterns of inter-seismic fault coupling before large
32 earthquakes (Perfettini and Avouac, 2004; Mavrommatis et al., 2014; Yokota and Koketsu,
33 2015) or during the post-seismic response of nearby large earthquakes (Heki and Mitsui,
34 2013; Melnick et al., 2017).

35 Although the existence of an anomalously large co-seismic slip associated with a su-
36 percycle behaviour is plausible, other studies suggest that the seismic moment of the 2016
37 Pedernales earthquake is actually consistent with the strain accumulated in the region since
38 the 1942 and 1906 earthquakes (e.g., Ye et al., 2016; Yoshimoto et al., 2017; Yi et al., 2018).
39 These contrasting statements partly results from the ill-posed nature of inter- and co-seismic
40 slip inversions used to evaluate the strain budget along the megathrust. Such inferences
41 are affected by the lack of resolution near the trench during the inter-seismic period but
42 also by non-physics-based smoothing constraints used to regularize slip inversions. In ad-
43 dition, inter- and co-seismic estimates usually do not incorporate rigorous uncertainties (or
44 very often, no uncertainty at all), which complicates a quantitative assessment of the overall
45 strain budget. Strain budget analyses also suffer from the lack of information about past

46 earthquakes (Yi et al., 2018). Incorrect considerations on the size and position of historical
47 events can strongly affect the conclusion on the strain state of the plate boundary.

48 We propose a probabilistic exploration of the Colombia-Ecuador earthquake sequence,
49 fully accounting for uncertainties, including measurement errors, modeling errors, but also
50 uncertainties in the location or magnitude of past events. Using a Bayesian framework,
51 we explore both the inter-seismic geodetic coupling of the subduction interface and the co-
52 seismic slip distribution of the $M_W=7.8$ Pedernales earthquake. These estimates do not rely
53 on any spatial smoothing and provide full posterior probability distributions describing the
54 ensemble of plausible models that fit the observations and are consistent with simple prior
55 constraints (e.g., slip positivity in the direction of convergence).

56 **2. Geodetic coupling**

57 *2.1. Stochastic inter-seismic modeling*

58 We first compute a stochastic model of geodetic coupling along the Ecuadorian subduc-
59 tion interface. We use inter-seismic GPS velocities computed by Chlieh et al. (2014) and
60 Nocquet et al. (2014) from 29 stations installed in Ecuador and Colombia and measured
61 from 1994 to 2012 (Mothes et al., 2018; Mora-Páez et al., 2018). Considering that more
62 than 20 years separate the 1979 earthquake and the first GPS measures, it is unlikely that
63 they are significantly affected by post-seismic deformation. The 1998 earthquake having a
64 smaller magnitude, its impact on the data is also probably minimal. The fault geometry
65 is based on a 3D surface following the Slab1.0 interface and discretized in triangles (c.f.,
66 Fig. S1 in the electronic supplements). Using a back-slip approach (Savage, 1983), we in-

77 vert for the inter-seismic slip rate along the direction of convergence between Nazca and
 78 North Andean Sliver (NAS) plates at each of the triangle knots assuming a barycentric in-
 79 terpolation scheme within the triangles. This approach avoids unphysical slip discontinuities
 80 associated with traditional parameterizations based on sub-faults with piecewise constant
 81 slip (Ortega Culaciati, 2013).

82 In our Bayesian inversion framework, the solution is the posterior ensemble of all plausible
 83 inter-seismic slip rate models ($\mathbf{m}_{\mathcal{I}}$) that fit the GPS data ($\mathbf{d}_{\mathcal{I}}$) and that are consistent
 84 with our prior hypotheses. This solution does not rely on any smoothing regularization
 85 and is based on a simple uniform prior for the inter-seismic slip-rate that writes $p(\mathbf{m}_{\mathcal{I}}) =$
 86 $\mathcal{U}(-0.05 \cdot V_p, 1.05 \cdot V_p)^M$ where V_p is the plate rate and M is the number of triangle knots
 87 (260 knots). We thus restrict our posterior PDF to models in which slip on the fault aligns
 88 with the direction of plate motion. Following Bayes' theorem, the posterior PDF is given by

$$p(\mathbf{m}_{\mathcal{I}}|\mathbf{d}_{\mathcal{I}}) \propto p(\mathbf{m}_{\mathcal{I}}) \exp \left[-\frac{1}{2}(\mathbf{d}_{\mathcal{I}} - \mathbf{G}_{\mathcal{I}}\mathbf{m}_{\mathcal{I}})^T \mathbf{C}_{\mathcal{I}}^{-1}(\mathbf{d}_{\mathcal{I}} - \mathbf{G}_{\mathcal{I}}\mathbf{m}_{\mathcal{I}}) \right] \quad (1)$$

89 where $\mathbf{G}_{\mathcal{I}}$ is the Green's function matrix and $\mathbf{C}_{\mathcal{I}}$ is the misfit covariance matrix combining
 90 observational errors and prediction uncertainties. Green's functions are computed for a semi-
 91 infinite stratified elastic medium derived from regional velocity models shown in Fig. S2
 92 (Béthoux et al., 2011; Vallee et al., 2013; Nocquet et al., 2017). We account for prediction
 93 uncertainties due to inaccuracies in this layered model using the approach of Duputel et al.
 94 (2012, 2014). The uncertainty on the elastic structure, presented as grey histograms in
 95 Fig. S2, is estimated by comparing previously published models in the region.

96 We sample the posterior PDF $p(\mathbf{m}_{\mathcal{I}}|\mathbf{d}_{\mathcal{I}})$ using AlTar, a parallel Markov Chain Monte

87 Carlo (MCMC) algorithm following the CATMIP algorithm (Minson et al., 2013). More
88 details on the application of AlTar to investigate inter-seismic deformations can be found in
89 Jolivet et al. (2015b) and Klein et al. (2017). The resulting posterior ensemble of slip-rate
90 models in eq. (1) is then converted into stochastic coupling maps (\mathbf{m}_C) using $\mathbf{m}_C = 1 - \mathbf{m}_I/V_p$.

91 *2.2. Geodetic coupling results*

92 Using our Bayesian framework, we generate 160 000 models corresponding to the posterior
93 information on geodetic coupling given measured inter-seismic velocities. We find that this
94 number is large enough to converge toward the posterior probability density. Representing
95 the ensemble of posterior models is challenging for multidimensional problems such as those
96 addressed in this study. To represent an ensemble solution, a common choice is to compute
97 the posterior mean (i.e., the average of all model samples). The posterior mean coupling
98 model is shown in Fig. 1 and Fig. 2a along with the associated $2\text{-}\sigma$ posterior uncertainties
99 in Fig. 2b. The posterior median model available in Fig. S3 is very similar to the posterior
100 mean, confirming that most marginal PDFs are nearly Gaussians. The variability of the
101 model population composing the solution is shown in supplementary movie M1.

102 Several features in our solution can be observed in previously published geodetic coupling
103 models (e.g., Nocquet et al., 2014; Chlieh et al., 2014). In the South, there is a very clear
104 high-coupling area offshore the Manta peninsula. This inter-seismically highly coupled region
105 has been previously associated with transient slow-slip events (Vallee et al., 2013; Nocquet
106 et al., 2014). As shown in Fig. 2a and Fig. 2e, this area is associated with small model
107 uncertainties probably because a GPS station is located on La Plata Island, right above the

108 coupled asperity. This coupled patch is bounded to the north by a low-coupling corridor
 109 that might have acted as a creeping barrier for the 1906, 1942, 1998 and 2016 earthquakes
 110 (cf., Fig. 1; Chlieh et al., 2014).

111 North of Bahía de Caráquez, we infer multiple patches of high geodetic coupling. Other
 112 coupled patches can be identified offshore of Bahía de Caráquez, North and South of Ped-
 113 ernales, and far offshore Esmeraldas. To first order, such heterogeneity is consistent with
 114 the "unsmoothed" solution of (Chlieh et al., 2014). This is unsurprising since our modeling
 115 approach is not affected by any prior-induced spatial smoothing. The high coupling asper-
 116 ity directly offshore of Bahía de Caráquez probably ruptured individually during the 1998
 117 $M_W=7.2$ earthquake while the coupled areas closer to Pedernales could have failed during
 118 the 1942 and 2016 earthquake (Fig. 1). On the other hand, the large region of high coupling
 119 between Esmeraldas and Cap Manglares could be involved in the 1958 and 1979 ruptures
 120 (cf., Fig. 1).

121 However, we observe larger model uncertainties in this northern part due the lack of
 122 offshore measurements (Fig. 2b). This is quite clear in Fig. 2e showing that marginal PDFs
 123 close to the trench are nearly uniform. Coupling uncertainties are also illustrated in the
 124 supplementary movie M1 showing that large variations in our model ensemble can fit the
 125 GPS observations equally well. To quantify the robustness of our coupling map, we calcu-
 126 late the information gain from prior to posterior marginal PDFs using the Kullback-Leibler
 127 divergence, defined as:

$$D_{KL}^i = \int p(m_c^i | \mathbf{d}_c) \log_2 \frac{p(m_c^i)}{p(m_c^i | \mathbf{d}_c)} dm_c^i \quad (2)$$

128 where m_c^i is the coupling sampled in i -th knot of the triangular mesh. The resulting map
129 shown in Fig. 2c, indicates how much information is gained from the data in different regions
130 of the model. It illustrates the difficulty to infer coupling properties close to the trench using
131 land-based geodetic data. Still, the information gain remains significant within 30-40 km of
132 the coast, and even sometimes almost up to the trench (e.g., offshore of the Manta peninsula
133 and between Esmeraldas and Cap Manglares). This suggests that aforementioned asperities
134 are reliable features of our solution. To evaluate the impact of the mesh size on our solution,
135 we have conducted an inversion using a coarser fault discretization (cf., Fig. S4). Because the
136 heterogeneities visible in Fig.2 are also present for that coarse parameterisation, we chose
137 the finer one to get a better spatial resolution and avoid any bias due to a coarse fault
138 discretization.

139 **3. Rupture process of the 2016 Pedernales earthquake**

140 *3.1. Data overview*

141 We use several geodetic datasets covering both near-field and far-field static displace-
142 ments (cf., Fig. 3a). We gather GPS data from 12 campaign stations and 14 permanent
143 stations with daily solutions (CGPS; Mothes et al., 2018), and 8 high-rate stations (HRGPS;
144 Alvarado et al., 2018) . Static offsets from campaign and permanent stations are provided by
145 Nocquet et al. (2017). We estimate our own static displacements from HRGPS by measuring
146 co-seismic offsets from the position before and after the event. We use $1\text{-}\sigma$ errors provided
147 by Nocquet et al. (2017) for the campaign and CGPS and estimate uncertainties for HRGPS
148 offsets from the standard deviation measured in 20 seconds pre- and post-event time win-

149 dows. Vertical components of campaign GPS are not used in the inversion as they show large
150 uncertainties. In addition, we use three interferograms derived from ALOS-2 wide-swath de-
151 scending acquisitions, from ALOS-2 strip-map ascending acquisitions and from Sentinel 1
152 descending acquisitions (cf., Fig. 4). Unwrapped interferograms are downsampled using a
153 quad-tree algorithm (cf., Fig. S5; Lohman and Simons, 2005). We estimate uncertainties
154 related to atmospheric noise by estimating empirical covariance functions for each interfer-
155 ogram (Jolivet et al., 2012, 2015a). Estimated parameters are summarized in Table S1 and
156 covariance functions are available in Fig. S6.

157 Three nearby DART buoys (Deep-ocean Assessment and Reporting of Tsunamis) recorded
158 the tsunami generated by this event. Unfortunately, the waveform recorded by the closest
159 station (D32067) is unusable for modeling because of multiple data gaps and contamina-
160 tion by seismic waves. We use tsunami waveforms recorded at DART stations D32413 and
161 D32411 (cf., Fig. 3b), as they provide important constraints on the up-dip part of the
162 rupture. To remove tidal signals and reduce high-frequency noise, we band-pass filter the
163 waveforms between 8 min and 3 hours using a third order Butterworth filter. We derive
164 observational uncertainties from standard deviations computed in 140 and 100 min windows
165 before the first arrivals respectively for buoys D32413 and D32411.

166 We also include near-field seismic waveforms recorded by 10 strong-motion accelerome-
167 ters and 8 HRGPS stations (c.f. Figs. 5 and 6; Alvarado et al., 2018). We integrate the
168 accelerometric data twice and downsample them to 1 sps to match the HRGPS sampling
169 rate. Waveforms are bandpass filtered between 0.015 Hz and 0.08 Hz, except for a few noisy

170 records for which we increased the lower corner frequency to 0.037 Hz (Table S2). Wave-
 171 forms are inverted in a 150 s-long time window starting from the origin time of the mainshock
 172 (23:58:36 UTC).

173 3.2. Stochastic co-seismic modeling

174 Our kinematic modeling of the 2016 Pedernales earthquake is based on a non-planar fault
 175 geometry in which the dip varies from 10° to 27° between 10 and 50 km depth, following the
 176 bending of the Slab1.0 model (cf., Fig. S7; Hayes et al., 2012). The fault is discretized in
 177 15×15 km patches in which we sample static (\mathbf{m}_S) and kinematic (\mathbf{m}_K) model parameters.
 178 The static model vector \mathbf{m}_S includes two components of static slip in each patch (i.e., the
 179 final integrated slip) and extra nuisance parameters to account for InSAR orbital errors (i.e.,
 180 3 parameters per interferogram to model a linear function of range and azimuth). The two
 181 components of static slip are U_{\parallel} , aligned with the direction of convergence between Nazca
 182 and NAS plates, and U_{\perp} , which is perpendicular to U_{\parallel} . The vector of kinematic parameters
 183 \mathbf{m}_K includes rupture velocity and rise time in each patch, along with hypocenter coordinates
 184 (i.e., the point of rupture initiation). Each point on the fault is only allowed to rupture once
 185 during the earthquake and we prescribe a triangular slip velocity function.

186 Following the approach of Minson et al. (2013), we first solve the final static slip distribu-
 187 tion (i.e., \mathbf{m}_S) given available static observations (\mathbf{d}_S), i.e., InSAR, GPS offsets and tsunami
 188 data. Using AlTar, we thus sample the posterior distribution:

$$\begin{aligned}
 p(\mathbf{m}_S | \mathbf{d}_S) &\propto p(\mathbf{m}_S) p(\mathbf{d}_S | \mathbf{m}_S) \\
 &\propto p(\mathbf{m}_S) \exp \left[-\frac{1}{2} (\mathbf{d}_S - \mathbf{G}_S \mathbf{m}_S)^T \mathbf{C}_S^{-1} (\mathbf{d}_S - \mathbf{G}_S \mathbf{m}_S) \right]
 \end{aligned}
 \tag{3}$$

189 where \mathbf{G}_S is the matrix including Green’s functions that are computed using the same
190 layered elastic medium than the one used for the inter-seismic coupling model (cf., section 2).
191 Tsunami waveforms are simulated using COMCOT (Liu et al., 1998) assuming a time step of
192 1 sec and a 30-arc second GEBCO (General Bathymetric Chart of the Oceans) bathymetry.
193 (Weatherall et al., 2015). As in eq. (1), the misfit covariance \mathbf{C}_S describes observational errors
194 and prediction uncertainties due to inaccuracies of the assumed elastic structure (Duputel
195 et al., 2012, 2014). As we want to promote a dominant thrust motion while allowing local
196 variations of the slip direction, the prior PDF $p(\mathbf{m}_S)$ includes uniform prior $\mathcal{U}(-1 \text{ m}, 15 \text{ m})$
197 along the direction of convergence (U_{\parallel}) and Gaussian prior $\mathcal{N}(0, 0.5 \text{ m})$ in the perpendicular
198 direction (U_{\perp}).

In a second step, we address the full joint inversion problem by incorporating kinematic
observations \mathbf{d}_K . HRGPS and strong motion data provide information on kinematic pa-
rameters \mathbf{m}_K and bring additional constraints on \mathbf{m}_S . The posterior PDF is then given by
(Minson et al., 2013):

$$\begin{aligned}
p(\mathbf{m}_S, \mathbf{m}_K | \mathbf{d}_S, \mathbf{d}_K) &\propto p(\mathbf{m}_K) p(\mathbf{m}_S | \mathbf{d}_S) p(\mathbf{d}_K | \mathbf{m}_S, \mathbf{m}_K) \\
&\propto p(\mathbf{m}_K) p(\mathbf{m}_S | \mathbf{d}_S) \exp \left[-\frac{1}{2} (\mathbf{d}_K - \mathbf{g}_K(\mathbf{m}_S, \mathbf{m}_K))^T \mathbf{C}_K^{-1} (\mathbf{d}_K - \mathbf{g}_K(\mathbf{m}_S, \mathbf{m}_K)) \right]
\end{aligned}
\tag{4}$$

199 where $\mathbf{g}_K(\mathbf{m}_S, \mathbf{m}_K)$ is the (non-linear) forward predictions for HRGPS and strong motion
200 waveforms that are based on the Herrmann (2013) implementation of the discrete wave-
201 number method (Bouchon and Aki, 1977). As in eq. (3), \mathbf{C}_K is the misfit covariance de-
202 scribing measurement errors and predictions uncertainties due to Earth model inaccuracies.
203 The prior $p(\mathbf{m}_K)$ is a combination of uniform priors $\mathcal{U}(1 \text{ s}, 12 \text{ s})$ and $\mathcal{U}(1 \text{ km/s}, 4 \text{ km/s})$ for

204 rise-time and rupture velocity and a Gaussian PDF $\mathcal{N}(\mathbf{x}_h, \sigma = 5 \text{ km})$ for the hypocenter
205 coordinates (\mathbf{x}_h).

206 *3.3. Co-seismic modeling results*

207 The Pedernales rupture is mainly unidirectional with a significant southward directivity
208 (see posterior mean model in Fig. 7, cumulative slip snapshots in Fig. 8, and supplementary
209 movie M2; Ye et al., 2016; Nocquet et al., 2017; Yi et al., 2018). The inverted hypocenter
210 (0.31° N , -80.15° W , depth=19.6 km; indicated by the red star in Fig. 7), is consistent with
211 estimates from the Instituto Geofísico de la Escuela Politécnica Nacional (0.35° N , -80.16° W ,
212 depth=17.0 km; <http://www.igepn.edu.ec>). Our solution depicts two large slip asperities
213 separated by ~ 50 km that coincides roughly with two high-coupling zones north and south
214 of the equator in Fig. 1 and supplementary movie M1. The first asperity is located close to
215 the epicenter and fails within 15 s after the origin time (Fig. 8). The second slip asperity
216 ruptures about 10 s later and contributes to more than 60% of the total seismic moment.
217 The rupture directivity and the location of the southernmost asperity, with slip up to 8 m
218 below the coastline, can probably explain the large damages that have been reported south
219 of the city of Pedernales (Nocquet et al., 2017).

220 Posterior model uncertainties indicate that we have good constraints on slip amplitude
221 through the fault plane (Fig. 7b and supplementary movie M3). Moreover, stochastic rupture
222 fronts presented in Fig. 7a show that rupture initiation times are well resolved in large
223 slip areas. There is however a tradeoff between rupture initiation times and rise times as
224 illustrated in Fig. 7c-d. This is because our seismic observations are mostly sensitive on

225 subfault centroid times rather than on rupture times and rise times, resulting in a negative
226 correlation with a -1 slope between the two later parameters.

227 The southward directivity is clearly visible on HRGPS and strong motion data that show
228 large ground motion amplitudes south of the rupture. This is well captured by our stochastic
229 model predictions (Figs. 5 and 6). Some discrepancies are visible in the late arrivals, which
230 are probably due to unaccounted 3D heterogeneities. Geodetic measurements provide good
231 constraints on the static slip pattern, with large static displacements observed above the
232 large slip asperity in the south. Our solution is able to predict GPS measurements (Fig. 3a)
233 and InSAR data, with small residuals for Sentinel and ALOS-2 data (Fig. 4). We notice
234 larger misfits for the ALOS-2 descending track, probably due to atmospheric noise since
235 this interferogram is associated with significant spatially-correlated observational noise (cf.,
236 Fig. S6). Our solution also provides satisfactory fit to tsunami waveforms despite their
237 relatively small amplitude (<1 cm, Fig. 3b). These tsunami observations are important since
238 they clearly show the absence of slip in the shallow portion of the fault (shallow slip would
239 produce large amplitude waves arriving too early at DART stations). This is also reported by
240 Ye et al. (2016) that conducted trial and error teleseismic inversions, progressively removing
241 shallow rows of patches to match the onset of tsunami signals.

242 **4. Strain budget along the Colombia-Ecuador subduction zone**

243 The Colombia-Ecuador subduction zone provides an outstanding opportunity to study
244 the behaviour of a megathrust fault over multiple earthquake cycles. As mentioned above,
245 before the 2016 Pedernales earthquake, the subduction interface experienced a sequence of

246 megathrust ruptures that started with a large $M_W=8.6$ event in 1906 followed by a series
 247 of smaller earthquakes in 1942, 1958, 1979 and 1998. Because these events seem to cluster
 248 in time, it has been suggested that strain released by most recent earthquakes exceeds the
 249 deformation that accumulated inter-seismically since 1906 (Nocquet et al., 2017; Yi et al.,
 250 2018).

251 The strain budget along the megathrust can be investigated by comparing the co-seismic
 252 moment generated by earthquakes with the moment deficit accumulated during previous
 253 inter-seismic periods. We define the moment deficit accumulated over an inter-seismic time-
 254 span T over an area A of a fault as:

$$M_0^{deficit} = T V_p \iint_A \mu(\mathbf{x}) m_c(\mathbf{x}) d\mathbf{x} \quad (5)$$

255 where V_p is the long-term convergence rate, $\mu(\mathbf{x})$ is the shear modulus along the subduction
 256 interface and $m_{\mathcal{I}}(\mathbf{x})$ is the coupling model introduced in section 2. Using such approach,
 257 Nocquet et al. (2017) propose that the co-seismic moment of the 1942 and 2016 earthquakes
 258 are much larger than the deficit accumulated since the 1906 earthquake (by a factor of 3 to
 259 5 times for the 1942 event and 1.3 to 1.6 times for 2016). This seems also true for northern
 260 segments and in particular for the 1958 earthquake that has a seismic moment 1.5 to 1.8
 261 times larger than the moment deficit estimated from the modeling of geodetic coupling. As
 262 discussed by Nocquet et al. (2017) and Yi et al. (2018), these estimates remain questionable
 263 given uncertainties on co-seismic slip and inter-seismic coupling.

264 Hereafter, we use our stochastic co-seismic and inter-seismic solutions to fully account
 265 for posterior uncertainties and address the strain budget probabilistically. We assume a

266 magnitude of $M_W=7.8 \pm 0.2$ for the 1942 earthquake (Swenson and Beck, 1996; Ye et al.,
267 2016). We compare the probability distributions of seismic moment generated by the 1942
268 and 2016 earthquakes with the moment deficit accumulated since 1906 (Fig. 9). Assuming
269 the two events are co-located, maximum a posteriori models indicate that the seismic moment
270 for the 1942 and 2016 events are larger than the accumulated deficit by a factor of 2.0 and 1.2,
271 respectively. Taken together for the 1906-2016 period, the moment generated co-seismically
272 is 1.3 times larger than the moment deficit accumulated inter-seismically. Those estimates
273 are subject to considerable uncertainties reflected by the overlap between the PDFs (Fig. 9).
274 Although this overlap is not negligible, there is a relatively small probability of about 5% to
275 have a moment deficit larger or equal than the cumulative seismic moment of the 1942 and
276 2016 earthquakes. In this scenario, an excess of co-seismic moment since 1906 is likely given
277 available observations.

278 This conclusion only holds if the 2016 rupture largely overlaps with the 1942 earth-
279 quake, whose location is still debated. In particular, Yi et al. (2018) suggests that the
280 1942 earthquake occurred at shallower depth than the 2016 rupture from the comparison
281 of macroisoseismic maps of 1942 and 1958 events (Swenson and Beck, 1996). Therefore we
282 test the alternative hypothesis suggesting that the 1942 earthquake occurred between lat
283 0.5°S - 0.5°N at a depth shallower than 40 km (Nocquet et al., 2017). Fig. 10a,b shows that
284 the negative moment balance no longer holds. In this case, the probability of having a deficit
285 equivalent or larger than the co-seismic moment is larger than 70%. Fig. 10c,d shows that
286 this remains true if we further restrain the location of the 1942 event to be located updip of

287 the 2016 earthquake (as proposed by Yi et al., 2018).

288 We conducted a similar analysis for the 1958 northern Ecuador earthquake, assuming a
289 magnitude $M_W=7.6\pm 0.2$ (according to Ye et al., 2016). Maximum a posteriori models in
290 Fig. S9b show that the seismic moment generated by the 1958 earthquake is quite similar
291 to the accumulated deficit between 1906 and 1958. This contradicts with Nocquet et al.
292 (2017) that estimated that the 1958 earthquake had a seismic moment exceeding by 50% to
293 180% the moment accumulated inter-seismically. In our case, we clearly see that the PDF
294 of the moment deficit falls within uncertainties of the 1958 co-seismic moment. As shown
295 in Fig. S9, this still holds if we assume different location for the 1958 earthquake, which
296 discards the negative moment balance issue reported for 1942 and 2016 earthquakes.

297 5. Discussion and Conclusion

298 We develop stochastic models of the inter-seismic slip-rate along the Colombia-Ecuador
299 subduction and of the 2016 Pedernales earthquake, which provide new constraints on uncer-
300 tainties of inter- and co-seismic slip processes. Our results are to first order consistent with
301 some previously published models (e.g., Nocquet et al., 2017; Chlieh et al., 2014). In partic-
302 ular, our coupling model presented in Fig. 2 is similar to the "unsmoothed" model of Chlieh
303 et al. (2014) since it is not affected by smoothing regularization. Our solution clearly depicts
304 a heterogeneous coupling of the subduction interface (cf., Fig. 2). The heterogeneity of fault
305 coupling properties seems to be a common feature to many subduction zones (Avouac, 2015),
306 but is often blurred because of poor spatial resolution and smoothing constraints used in the
307 inversion. Despite large uncertainties due to the lack of geodetic observations far offshore,

308 all models in our posterior ensemble show a large spatial heterogeneity (cf., supplementary
309 movie M1).

310 Such heterogeneity roughly correlates with the spatial complexity of the 2016 earthquake
311 revealed by our co-seismic solution. Our results indicate a unidirectional rupture towards
312 the South with two large slip zones that coincide with two high-coupling asperities in the
313 inter-seismic solution (cf., Fig. 1). We evaluate the possibility that the seismic moment
314 generated by the 1942 and 2016 earthquakes is larger than the moment deficit accumulated
315 since the great 1906 earthquake (as suggested by Nocquet et al., 2017). Our analyses show
316 that this conclusion only holds if we assume that there is a large overlap between the 1942
317 and 2016 ruptures. If this particular assumption is loosened, results indicate that such an
318 unbalanced moment budget is no longer required by observations. North of the Pedernales
319 rupture, we also show that the seismic moment of the 1958 earthquake is not necessarily
320 larger than the deficit accumulated since 1906 given uncertainties in co- and inter-seismic
321 processes. The question therefore entirely lies within the accuracy of the location and extent
322 of historical earthquakes.

323 One of the previously mentioned argument favouring an overlap between 1942 and 2016
324 earthquakes comes from the analysis of teleseismic waveforms recorded at a similar location
325 for both events (see details in supplementary text T1). Ye et al. (2016) showed that 1942 and
326 2016 waveforms at the station DBN (De Bilt, Netherlands) present significant dissimilarities.
327 Fig. S10 shows that such discrepancies can be explained by differences in the hypocenter
328 location with the same slip distribution for both events (as previously suggested by Nocquet

329 et al., 2017). However, the shape of the observed teleseismic P-wave is mostly controlled
330 by the relative location between the hypocenter and the main slip asperities (i.e., by the
331 corresponding apparent moment-rate function). In fact, Fig. S10c shows that the 1942
332 DBN waveform could be explained equally well if we assume that the 1942 rupture occurred
333 updip of the 2016 earthquake as suggested by focal depth and macro-isoseismic maps of
334 the 1942 event (Yi et al., 2018). In this scenario, there is a probability of $\sim 70\%$ to have
335 a balanced moment budget since 1906 (i.e., a moment deficit that is larger or equal to
336 the seismic moment of 1942 and 2016 events). On the contrary, if there is a large overlap
337 between both earthquakes, our results show that there is a 95% probability that the moment
338 generated by 1942 and 2016 ruptures is larger than the moment deficit accumulated since
339 1906. In this case such an unbalanced moment budget can possibly be explained by temporal
340 variations in strain accumulation, which have been observed for example before and after the
341 2011 $M_W=9.0$ Tohoku earthquake (e.g., Mavrommatis et al., 2014; Heki and Mitsui, 2013)
342 and after the 2010 Maule earthquake (Melnick et al., 2017; Loveless, 2017). Alternatively,
343 Nocquet et al. (2017) propose a "supercycle" model where the apparent excess of co-seismic
344 moment results from the fact that the 1906 and 1942 earthquakes did not release all of the
345 accumulated strain along the megathrust. This is consistent with the modeling of historic
346 tsunami records suggesting that the 1906 earthquake mainly ruptured the shallow part of
347 the subduction without involving much slip close to the 2016 Pedernales event (Yoshimoto
348 et al., 2017). However, these estimates might be biased by the poor sensitivity of tsunami
349 data to deep slip, which can explain the relatively low magnitude of their resulting model

350 ($M_W=8.4$). The fact that the surface wave magnitude $M_s=8.6$ is otherwise consistent with
351 M_W also suggests that the 1906 earthquake is not a typical "tsunami" earthquake and is
352 therefore probably not associated with a predominantly shallow rupture (Kanamori, 1972).

353 The complex behaviour of the Colombia-Ecuador subduction can be related to the large
354 heterogeneity revealed by our coupling solution, which suggests significant spatial variability
355 of fault frictional properties (Fig. 1) Such frictional heterogeneities could result from spatial
356 variations in rheology, fluid pore pressure (e.g., Avouac, 2015) or fault roughness associated
357 with the subduction of topographic features such as ridges, fracture zones and seamounts
358 (Collot et al., 2017; Graindorge, 2004). As shown for example by Kaneko et al. (2010), such
359 frictional heterogeneity can produce earthquakes of different sizes re-rupturing the same
360 fault region at short time intervals. Complex earthquake sequences may also be promoted
361 by partial stress drop of past events that produces significant stress heterogeneity along the
362 fault (Cochard and Madariaga, 1996). The fact that large earthquakes (like the 1906 event)
363 are rapidly followed by sequences of smaller ruptures (e.g., in 1942, 1958, 1979, 1998 and
364 2016) can then be understood if static stress drop of the smaller events is small compared to
365 the increase of dynamic stresses at rupture fronts (Heaton, 1990; Melgar and Hayes, 2017).

366 As instrumental observations accumulate, there is a growing record of large earthquakes
367 that break portions of faults that experienced previously documented large ruptures. These
368 earthquakes continuously provide new observations suggesting complex earthquake sequences
369 with substantial spatial and temporal variability among successive ruptures of the same fault
370 system. As shown here, the study of long-term earthquake sequences and the associated

371 strain budget still relies on many assumptions and are affected by large uncertainties. To ad-
372 dress the seismogenic behaviour of active faults, we need to quantify how large observational
373 and modelling uncertainties are and how much information we have gained in comparison
374 to our preconceptions. Inaccuracies on historical earthquakes size and position can be sub-
375 stantial and also need to be properly considered. Such quantitative analysis is essential to
376 understand how strain accumulates inter-seismically and is released by earthquakes, thereby
377 improving seismic hazard assessment along subduction zones.

378 **6. Acknowledgment**

379 The ALOS-2 original data are copyright JAXA and provided under JAXA RA4 PI Project
380 P1372002. The Copernicus Sentinel-1 data were provided by the European Space Agency
381 (ESA). Contains modified Copernicus data 2016, processed by ESA and NASA/JPL. We
382 thank the Instituto Geofísico de la Escuela Politécnica Nacional (IG-EPN Ecuador) and the
383 IRD for making available the static GPS, high-rate GPS and accelerometers data used in this
384 study. Aside from the data from the IG-EPN and IRD networks, the data set also includes
385 accelerometer data from OCP and GPS data from the Instituto Geográfico Militar (IGM) and
386 Servicio Geológico Colombiano, Proyecto GeoRED from Colombia, that we also thank. The
387 waveform of the 1942 earthquake used on this study was provided by Lingling Ye and Hiroo
388 Kanamori. This project has received funding from the Agence Nationale de la Recherche
389 (ANR-17-ERC3-0010), the European Union’s Horizon 2020 research and innovation program
390 (grant agreement 758210), and the CNRS international program for scientific co- operation
391 (PICS). This research was also supported by the NASA Earth Surface and Interior focus

392 area and performed at the Jet Propulsion Laboratory, California Institute of Technology. We
393 thank the Editor, Jean-Philippe Avouac, and two anonymous reviewers for their constructive
394 comments, which helped improve this manuscript.

395 Alvarado, A., Ruiz, M., Mothes, P., Yepes, H., Segovia, M., Vaca, M., Ramos, C., Enríquez,
396 W., Ponce, G., Jarrín, P., et al. (2018). Seismic, volcanic, and geodetic networks in
397 Ecuador: Building capacity for monitoring and research. *Seismological Research Letters*,
398 89(2A):432–439.

399 Avouac, J.-P. (2015). From geodetic imaging of seismic and aseismic fault slip to dy-
400 namic modeling of the seismic cycle. *Annual Review of Earth and Planetary Sciences*,
401 43(1):233–271.

402 Beck, S. L. and Ruff, L. J. (1984). The Rupture Process of the Great 1979 Colombia
403 Earthquake - Evidence for the Asperity Model. *J. Geophys. Res.*, 89(NB11):9281–9291.

404 Béthoux, N., Segovia, M., Alvarez, V., Collot, J.-Y., Charvis, P., Gailler, A., and Monfret,
405 T. (2011). Seismological study of the central Ecuadorian margin: Evidence of upper plate
406 deformation. *J. South Amer. Earth Sci.*, 31(1):139–152.

407 Bouchon, M. and Aki, K. (1977). Discrete wave-number representation of seismic-source
408 wave fields. *Bulletin of the Seismological Society of America*, 67(2):259–277.

409 Chlieh, M., Mothes, P., Nocquet, J.-M., Jarrin, P., Charvis, P., Cisneros, D., Font, Y.,
410 Collot, J.-Y., Villegas-Lanza, J.-C., Rolandone, F., et al. (2014). Distribution of discrete
411 seismic asperities and aseismic slip along the Ecuadorian megathrust. *Earth and Planetary
412 Science Letters*, 400:292–301.

413 Cochard, A. and Madariaga, R. (1996). Complexity of seismicity due to highly

414 rate-dependent friction. *Journal of Geophysical Research: Solid Earth (1978–2012)*,
415 101(B11):25321–25336.

416 Collot, J.-Y., Sanclemente, E., Nocquet, J.-M., Lepretre, A., Ribodetti, A., Jarrin, P., Chlieh,
417 M., Graindorge, D., and Charvis, P. (2017). Subducted oceanic relief locks the shal-
418 low megathrust in central ecuador. *Journal of Geophysical Research: Solid Earth*, page
419 2016JB013849.

420 Duputel, Z., Agram, P. S., Simons, M., Minson, S. E., and Beck, J. L. (2014). Accounting for
421 prediction uncertainty when inferring subsurface fault slip. *Geophys. J. Int.*, 197(1):464–
422 482.

423 Duputel, Z., Rivera, L., Fukahata, Y., and Kanamori, H. (2012). Uncertainty estimations
424 for seismic source inversions. *Geophys. J. Int.*, 190(2):1243–1256.

425 Graindorge, D. (2004). Deep structures of the Ecuador convergent margin and the Carnegie
426 Ridge, possible consequence on great earthquakes recurrence interval. *Geophys. Res. Lett.*,
427 31(4):L04603.

428 Gutenberg, B. and Richter, C. F. (1949). *Seismicity of the Earth and Associated Phenomena*.
429 Princeton University Press, Princeton, New Jersey.

430 Hayes, G. P., Wald, D. J., and Johnson, R. L. (2012). Slab1.0: A three-dimensional model
431 of global subduction zone geometries. *J. Geophys. Res.: Solid Earth*, 117(B1).

432 He, P., Hetland, E. A., Wang, Q., Ding, K., Wen, Y., and Zou, R. (2017). Coseismic Slip

433 in the 2016 Mw 7.8 Ecuador Earthquake Imaged from Sentinel-1A Radar Interferometry.
434 *Seismol. Res. Lett.*, 88(2A):277–286.

435 Heaton, T. H. (1990). Evidence for and implications of self-healing pulses of slip in earthquake
436 rupture. *Physics of the Earth and Planetary Interiors*, 64(1):1–20.

437 Heki, K. and Mitsui, Y. (2013). Accelerated pacific plate subduction following interplate
438 thrust earthquakes at the Japan trench. *Earth Planet. Sci. Lett.*, 363:44–49.

439 Herrmann, R. B. (2013). Computer Programs in Seismology: An Evolving Tool for Instruc-
440 tion and Research. *Seismol. Res. Lett.*, 84(6):1081–1088.

441 Jacoby, G. C., Sheppard, P. R., and Sieh, K. E. (1988). Irregular Recurrence of Large
442 Earthquakes Along the San Andreas Fault: Evidence from Trees. *Science*, 241(4862):196–
443 199.

444 Jolivet, R., Candela, T., Lasserre, C., Renard, F., Klinger, Y., and Doin, M.-P. (2015a).
445 The Burst-Like Behavior of Aseismic Slip on a Rough Fault: The Creeping Section of the
446 Haiyuan Fault, China. *Bull. Seism. Soc. Am.*, 105(1):480–488.

447 Jolivet, R., Lasserre, C., Doin, M.-P., Guillaso, S., Peltzer, G., Dailu, R., Sun, J., Shen,
448 Z.-K., and Xu, X. (2012). Shallow creep on the Haiyuan fault (Gansu, China) revealed by
449 SAR interferometry. *Journal of Geophysical Research: Solid Earth*, 117(B6).

450 Jolivet, R., Simons, M., Agram, P., Duputel, Z., and Shen, Z.-K. (2015b). Aseismic slip and
451 seismogenic coupling along the central San Andreas Fault. *Geophysical Research Letters*,
452 42(2):297–306.

- 453 Kanamori, H. (1972). Mechanism of Tsunami Earthquakes. *Phys. Earth Planet. Inter.*,
454 6:356–359.
- 455 Kanamori, H. and McNally, K. C. (1982). Variable Rupture Mode of the Subduction Zone
456 Along the Ecuador - Colombia Coast. *Bull. Seism. Soc. Am.*, 72(4):1241–1253.
- 457 Kaneko, Y., Avouac, J.-P., and Lapusta, N. (2010). Towards inferring earthquake patterns
458 from geodetic observations of interseismic coupling. *Nature Geosci.*, 3(5):ngeo843–369.
- 459 Klein, E., Duputel, Z., Masson, F., Yavasoglu, H., and Agram, P. (2017). Aseismic slip
460 and seismogenic coupling in the Marmara Sea: What can we learn from onland geodesy?
461 *Geophys. Res. Lett.*, 44(7):3100–3108.
- 462 Lay, T. (2015). The surge of great earthquakes from 2004 to 2014. *Earth Planet. Sci. Lett.*,
463 409:133–146.
- 464 Liu, P. L. F., Woo, S.-B., and Cho, Y.-S. (1998). Computer Programs for Tsunami Propa-
465 gation and Inundation. Cornell University, USA.
- 466 Lohman, R. B. and Simons, M. (2005). Some thoughts on the use of InSAR data to con-
467 strain models of surface deformation: Noise structure and data downsampling. *Geochem.*
468 *Geophys. Geosyst.*, 6(1):Q01007.
- 469 Loveless, J. P. (2017). Super-interseismic periods: Redefining earthquake recurrence. *Geo-*
470 *phys. Res. Lett.*, 44(3):1329–1332.
- 471 Mavrommatis, A. P., Segall, P., and Johnson, K. M. (2014). A decadal-scale deforma-

472 tion transient prior to the 2011 Mw 9.0 Tohoku-oki earthquake. *Geophys. Res. Lett.*,
473 41(13):4486–4494.

474 Melgar, D. and Hayes, G. P. (2017). Systematic observations of the slip pulse properties of
475 large earthquake ruptures. *Geophysical Research Letters*, 44(19):9691–9698.

476 Melnick, D., Moreno, M., Quinteros, J., Baez, J. C., Deng, Z., Li, S., and Oncken, O. (2017).
477 The super-interseismic phase of the megathrust earthquake cycle in Chile. *Geophys. Res.*
478 *Lett.*, 44(2):784–791.

479 Mendoza, C. and Dewey, J. W. (1984). Seismicity Associated with the Great Colombia-
480 Ecuador Earthquakes of 1942, 1958, and 1979 - Implications for Barrier Models of Earth-
481 quake Rupture. *Bull. Seism. Soc. Am.*, 74(2):577–593.

482 Minson, S., Simons, M., and Beck, J. (2013). Bayesian inversion for finite fault earthquake
483 source models I Theory and algorithm. *Geophysical Journal International*, 194(3):1701–
484 1726.

485 Mora-Páez, H., Peláez-Gaviria, J.-R., Diederix, H., Bohórquez-Orozco, O., Cardona-
486 Piedrahita, L., Corchuelo-Cuervo, Y., Ramírez-Cadena, J., and Díaz-Mila, F. (2018).
487 Space geodesy infrastructure in Colombia for geodynamics research. *Seismological Re-*
488 *search Letters*, 89(2A):446–451.

489 Mothes, P. A., Rolandone, F., Nocquet, J.-M., Jarrin, P. A., Alvarado, A. P., Ruiz, M. C.,
490 Cisneros, D., Páez, H. M., and Segovia, M. (2018). Monitoring the earthquake cycle in

491 the northern Andes from the Ecuadorian cGPS network. *Seismological Research Letters*,
492 89(2A):534–541.

493 Nocquet, J. M., Jarrin, P., Vallée, M., Mothes, P. A., Grandin, R., Rolandone, F., Delouis,
494 B., Yepes, H., Font, Y., Fuentes, D., Regnier, M., Laurendeau, A., Cisneros, D., Hernan-
495 dez, S., Sladen, A., Singaicho, J. C., Mora, H., Gomez, J., Montes, L., and Charvis, P.
496 (2017). Supercycle at the Ecuadorian subduction zone revealed after the 2016 Pedernales
497 earthquake. *Nature Geoscience*, 10(2):145–149.

498 Nocquet, J. M., Villegas-Lanza, J. C., Chlieh, M., Mothes, P. A., Rolandone, F., Jarrin, P.,
499 Cisneros, D., Alvarado, A., Audin, L., Bondoux, F., Martin, X., Font, Y., Regnier, M.,
500 Vallée, M., Tran, T., Beauval, C., Mendoza, J. M. M., Martinez, W., Tavera, H., and
501 Yepes, H. (2014). Motion of continental slivers and creeping subduction in the northern
502 Andes. *Nature Geosci.*, 7(4):287–291.

503 Ortega Culaciati, F. H. (2013). *Aseismic Deformation in Subduction Megathrusts: Central*
504 *Andes and North-East Japan*. PhD thesis, California Institute of Technology, Pasadena,
505 CA, USA.

506 Perfettini, H. and Avouac, J. P. (2004). Stress transfer and strain rate variations during the
507 seismic cycle. *J. Geophys. Res.: Solid Earth*, 109(B6).

508 Savage, J. (1983). A dislocation model of strain accumulation and release at a subduction
509 zone. *Journal of Geophysical Research: Solid Earth*, 88(B6):4984–4996.

510 Schwartz, D. P. and Coppersmith, K. J. (1984). Fault behavior and characteristic earth-

511 quakes: Examples from the Wasatch and San Andreas Fault Zones. *Journal of Geophysical*
512 *Research: Solid Earth (1978–2012)*, 89(B7):5681–5698.

513 Shimazaki, K. and Nakata, T. (1980). Time-predictable recurrence model for large earth-
514 quakes. *Geophys. Res. Lett.*, 7(4):279–282.

515 Sieh, K., Natawidjaja, D. H., Meltzner, A. J., Shen, C. C., Cheng, H., Li, K. S., Suwargadi,
516 B. W., Galetzka, J., Philibosian, B., and Edwards, R. L. (2008). Earthquake Supercy-
517 cles Inferred from Sea-Level Changes Recorded in the Corals of West Sumatra. *Science*,
518 322(5908):1674–1678.

519 Simons, M., Minson, S. E., Sladen, A., Ortega, F., Jiang, J., Owen, S. E., Meng, L., Ampuero,
520 J.-P., Wei, S., Chu, R., Helmberger, D. V., Kanamori, H., Hetland, E., Moore, A. W., and
521 Webb, F. H. (2011). The 2011 Magnitude 9.0 Tohoku-Oki Earthquake: Mosaicking the
522 Megathrust from Seconds to Centuries. *Science*, 332(6036):1421–1425.

523 Swenson, J. L. and Beck, S. L. (1996). Historical 1942 Ecuador and 1942 Peru subduc-
524 tion earthquakes and earthquake cycles along Colombia-Ecuador and Peru subduction
525 segments. *Pure appl. geophys.*, 146(1):67–101.

526 Vallee, M., Nocquet, J.-M., Battaglia, J., Font, Y., Segovia, M., Regnier, M., Mothes, P.,
527 Jarrin, P., Cisneros, D., Vaca, S., et al. (2013). Intense interface seismicity triggered by a
528 shallow slow slip event in the Central Ecuador subduction zone. *Journal of Geophysical*
529 *Research: Solid Earth*, 118(6):2965–2981.

530 Vallée, M. and Satriano, C. (2014). Ten year recurrence time between two major earthquakes
531 affecting the same fault segment. *Geophysical Research Letters*, 41(7):2312–2318.

532 Weatherall, P., Marks, K., Jakobsson, M., Schmitt, T., Tani, S., Arndt, J. E., Rovere, M.,
533 Chayes, D., Ferrini, V., and Wigley, R. (2015). A new digital bathymetric model of the
534 world’s oceans. *Earth and Space Science*, 2(8):331–345.

535 Ye, L., Kanamori, H., Avouac, J.-P., Li, L., Cheung, K. F., and Lay, T. (2016). The 16 April
536 2016, MW7.8 (MS7.5) Ecuador earthquake: A quasi-repeat of the 1942 MS7.5 earthquake
537 and partial re-rupture of the 1906 MS8.6 Colombia–Ecuador earthquake. *Earth Planet.*
538 *Sci. Lett.*, 454(Supplement C):248–258.

539 Yi, L., Xu, C., Wen, Y., Zhang, X., and Jiang, G. (2018). Rupture process of the 2016 Mw
540 7.8 Ecuador earthquake from joint inversion of InSAR data and teleseismic P waveforms.
541 *Tectonophysics*, 722:163–174.

542 Yokota, Y. and Koketsu, K. (2015). A very long-term transient event preceding the 2011
543 Tohoku earthquake. *Nature Communications*, 6:5934.

544 Yoshimoto, M., Kumagai, H., Acero, W., Ponce, G., Vásconez, F., Arrais, S., Ruiz, M.,
545 Alvarado, A., Pedraza García, P., Dionicio, V., Chamorro, O., Maeda, Y., and Nakano,
546 M. (2017). Depth-dependent rupture mode along the Ecuador-Colombia subduction zone.
547 *Geophys. Res. Lett.*, 84(5):1561–2210.

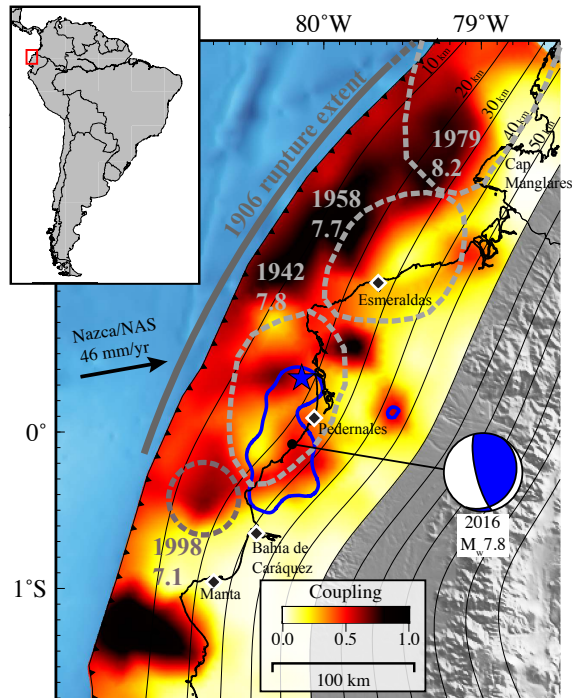


Figure 1: **Interseismic coupling and historical earthquakes.** The colour scale indicates the geodetic coupling of the subduction interface obtained from inter-seismic GPS velocities (cf. section 2). Blue line and blue star are respectively the 2 m isocontours of co-seismic slip and hypocenter obtained for the 2016 Pedernales earthquake (cf., section 3). Grey dashed lines show the approximate extent of the 1942, 1958, 1979, and 1998 events (Kanamori and McNally, 1982; Chlieh et al., 2014). The location of these previous ruptures is still debated, and some alternative plausible locations are shown in Fig. 10 and S9. The thick gray line shows the along-strike extent of the 1906 $M_W = 8.6$ earthquake. The focal mechanism of the 2016 Pedernales earthquake is presented in blue. Thin black lines are isocontours of the slab depth. The line with the adjacent black triangles shows the location of the trench. The black arrow illustrates the convergence direction of the Nazca plate toward the North Andean Silver plate (NAS, Chlieh et al., 2014).

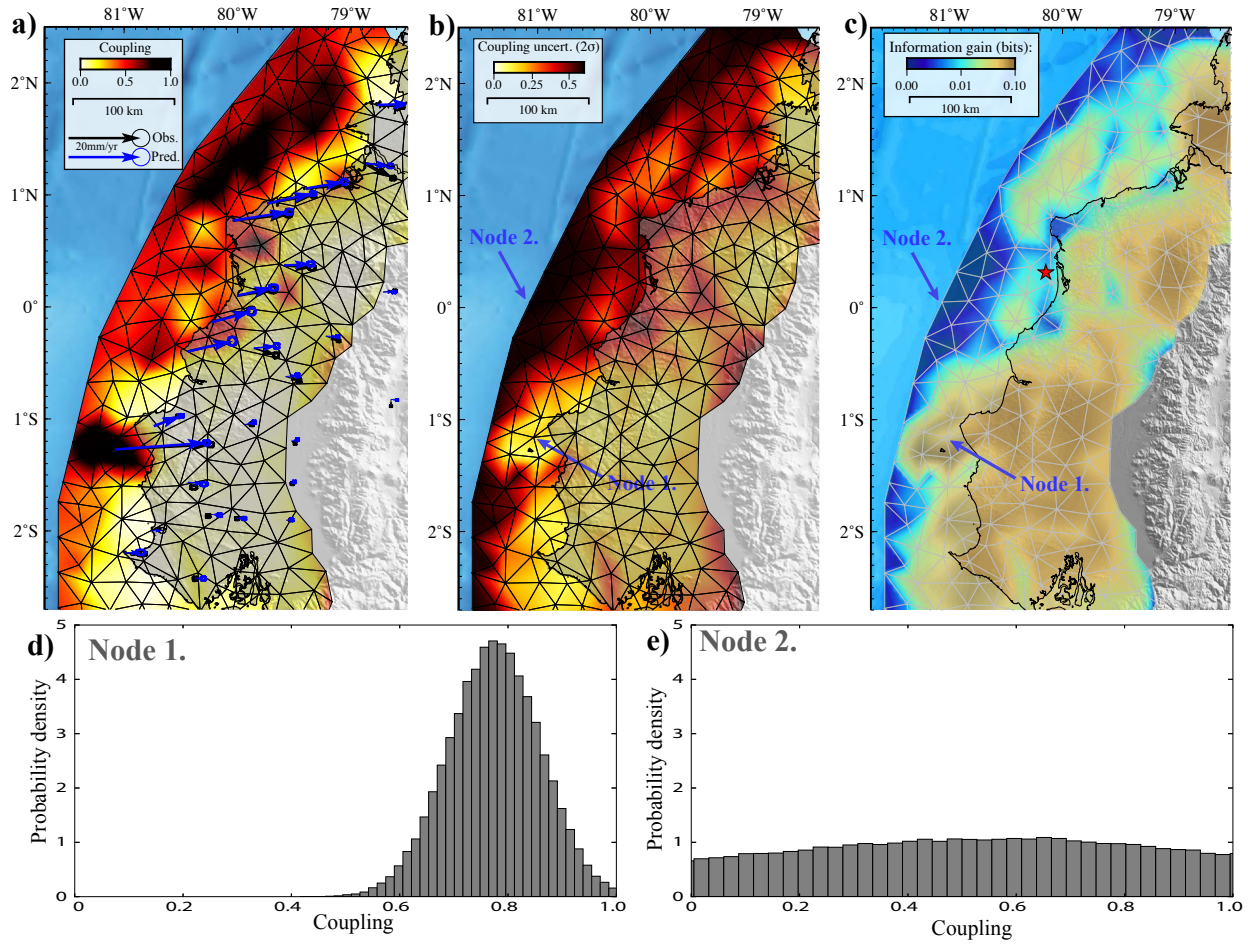


Figure 2: **Interseismic coupling of the Ecuadorian subduction margin.** a) Posterior mean coupling model. Thin black lines represent the fault parametrization. Coupling values are inverted at each triangle knot. Interseismic GPS displacement and model predictions are plotted as black and blue arrows, respectively. b) 2- σ uncertainties of the coupling model. c) Kullback-Leibler divergence between the posterior and prior PDFs of coupling. Higher values indicate regions where the gain of information of the posterior PDF is significant relative to the prior distribution. d) et e) Marginal probability densities for the two nodes pointed out in b) and c).

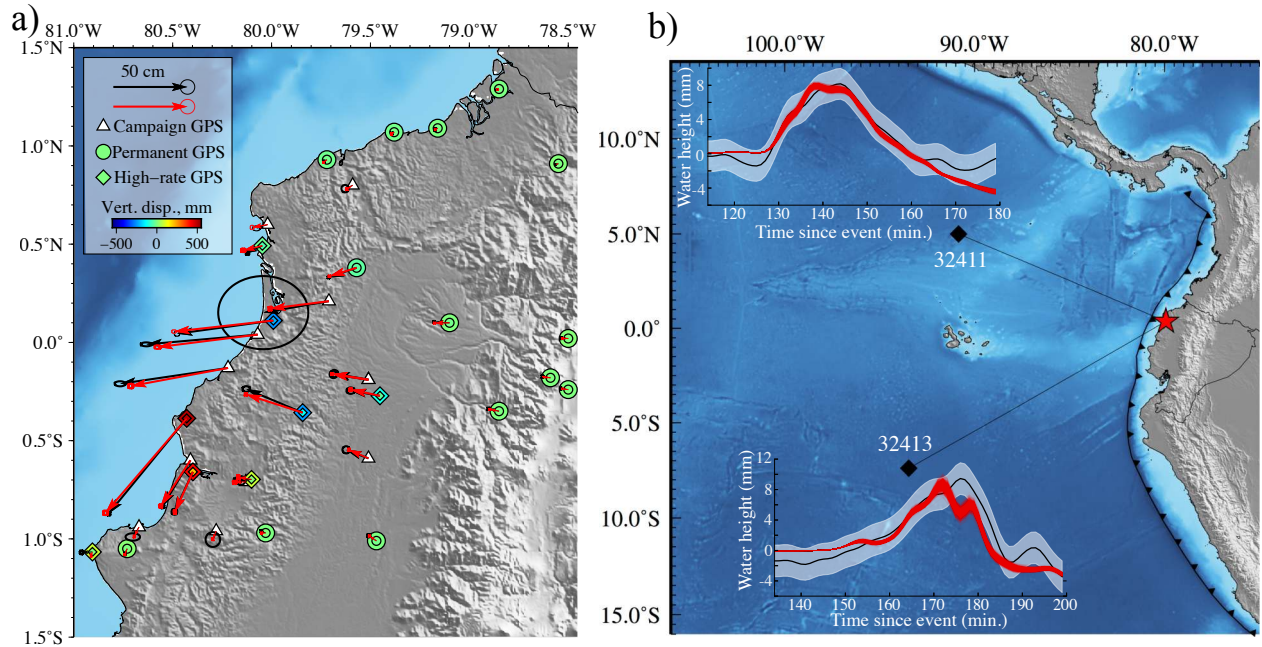


Figure 3: **GPS and tsunami observations used in this study.** **a)** GPS data and model predictions. Black and red arrows show observed and predicted GPS horizontal displacements along with their 95%-confidence ellipses (representing observational and prediction uncertainties, respectively). For the permanent and High-rate GPS, the symbol colour represents the vertical displacement. The outer symbol is the observation while the inner symbol is the mean model prediction. **b)** Observed and predicted tsunami waveforms. The red star defines the event epicenter while black diamonds are the locations of the two DART buoys that recorded the tsunami. For each of them, the amplitude of the first arrival is plotted as a thick black line. The surrounding shaded area marks the $2\text{-}\sigma$ confidence interval. Stochastic forward model predictions are plotted in red.

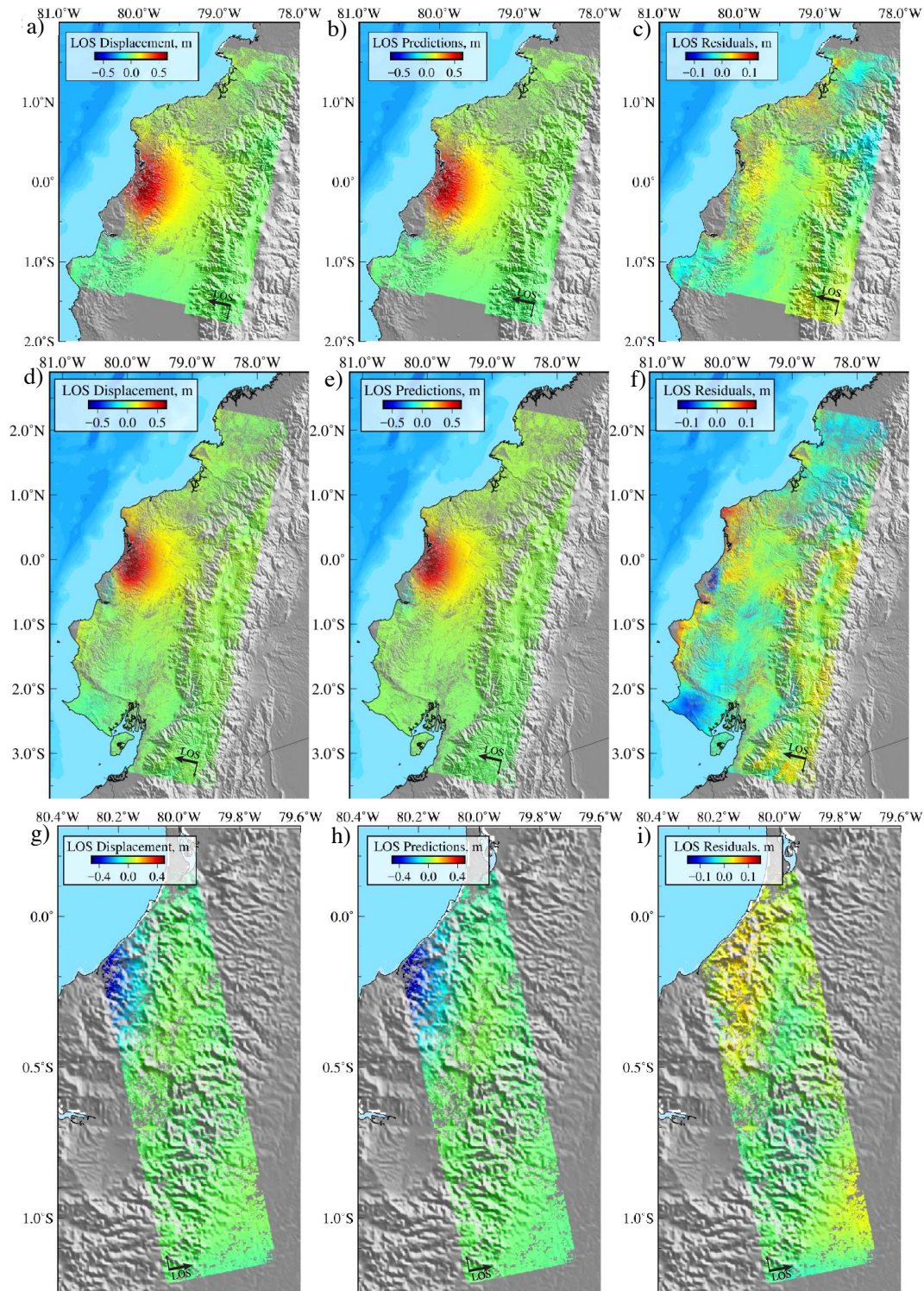


Figure 4: **Model performance for InSAR.** (a, d, g) InSAR observations. (b, e, h) Predictions for the posterior mean model. (c, f, i) Residuals of the Sentinel (top row), descending ALOS-2 wide-swath (middle row), and ascending ALOS-2 strip-map (bottom row) interferograms. Decimated observations, predictions, and residuals are shown in Fig. S5

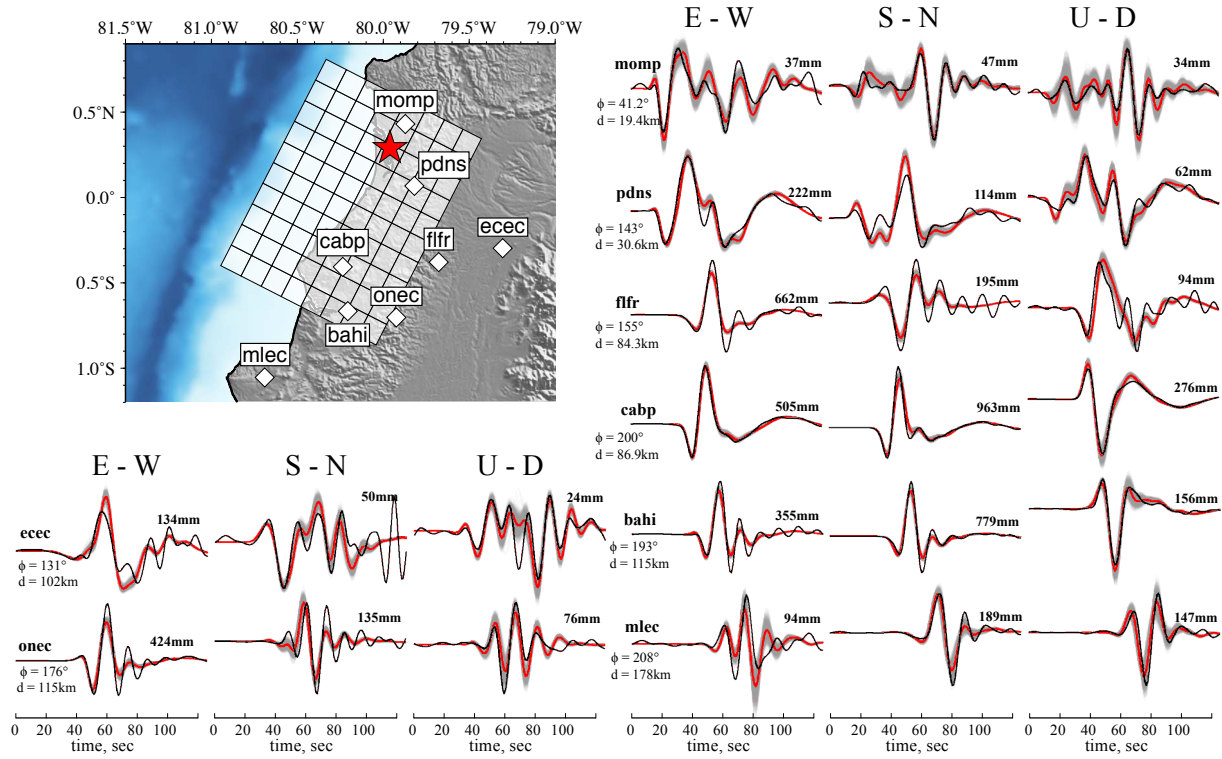


Figure 5: **High-rate GPS observations and model predictions.** The white diamonds on the top-left map indicate the position of the stations. The red star marks the inverted epicenter location. White rectangles are the fault parametrization. The East, North, and vertical components of each station are plotted around the map. For each waveform, the bold number indicates its maximum amplitude. The station azimuth Φ and distance d to the epicenter are also given. The black line is the recorded waveform. The gray lines are the stochastic predictions for our posterior model. The red line is the mean of the stochastic predictions.

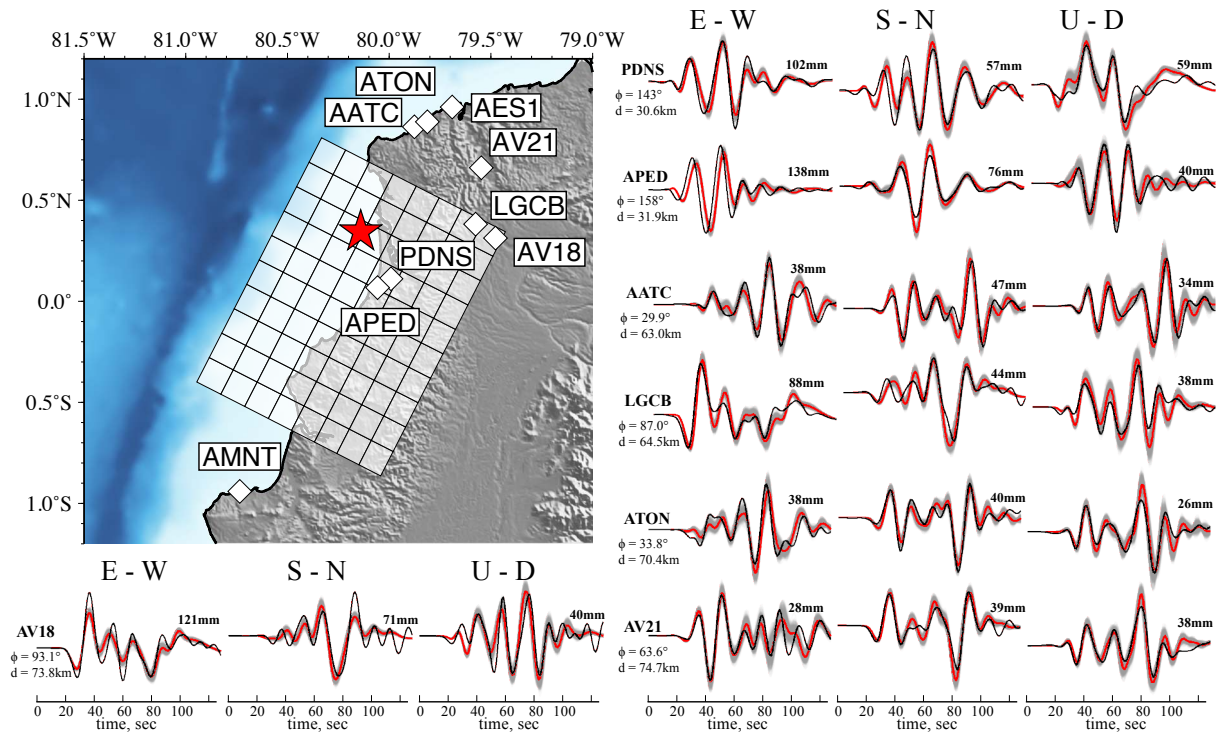


Figure 6: **Strong-motion observations and model predictions.** Same as Fig. 5. We show only the stations where three components are available. The remaining 5 waveforms from 3 additional stations and the associated model predictions are shown in Fig. S8

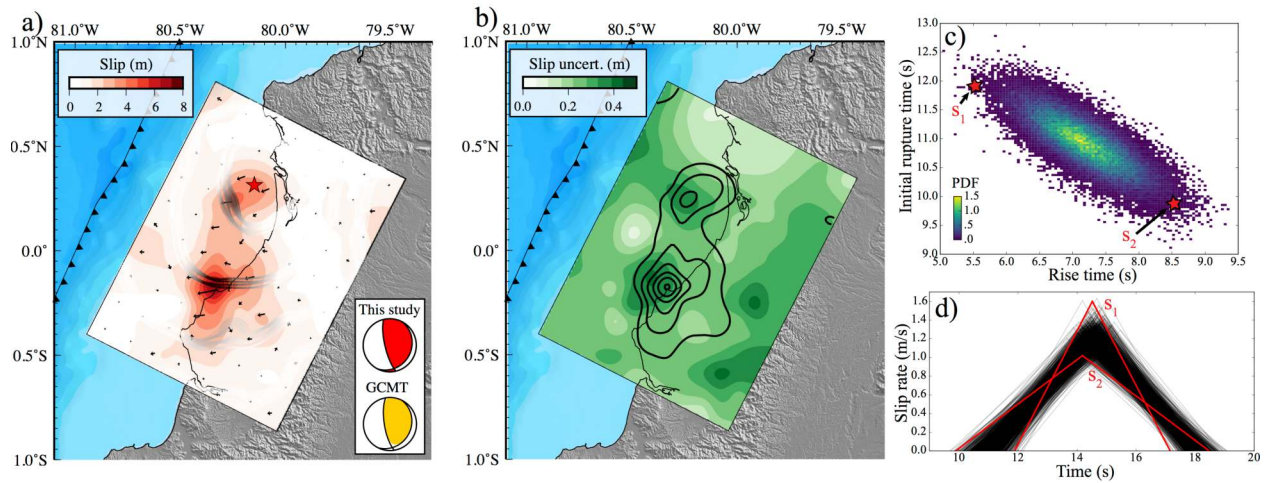


Figure 7: **Final co-seismic slip distribution.** **a)** The colour and arrows on the fault plane indicate the amplitude and direction of slip, respectively. Gray-scale lines are stochastic rupture fronts inferred from our model population plotted at 10s, 20s, and 30s. The darker the lines, the larger the slip at that location. The red star marks the hypocenter location. **b)** Slip uncertainty. The colour on the fault represents the absolute slip uncertainties. Black contour lines show the co-seismic slip every 1 m, starting from 2 m. **c)** Marginal probability distribution of rise time and initial rupture time in the first slip asperity (located close to the hypocenter). **d)** Posterior ensemble of source time functions at the same location of the fault. The source time functions labeled s_1 and s_2 in (d) correspond to rupture initiation times and rise times that are indicated with red stars in (c).

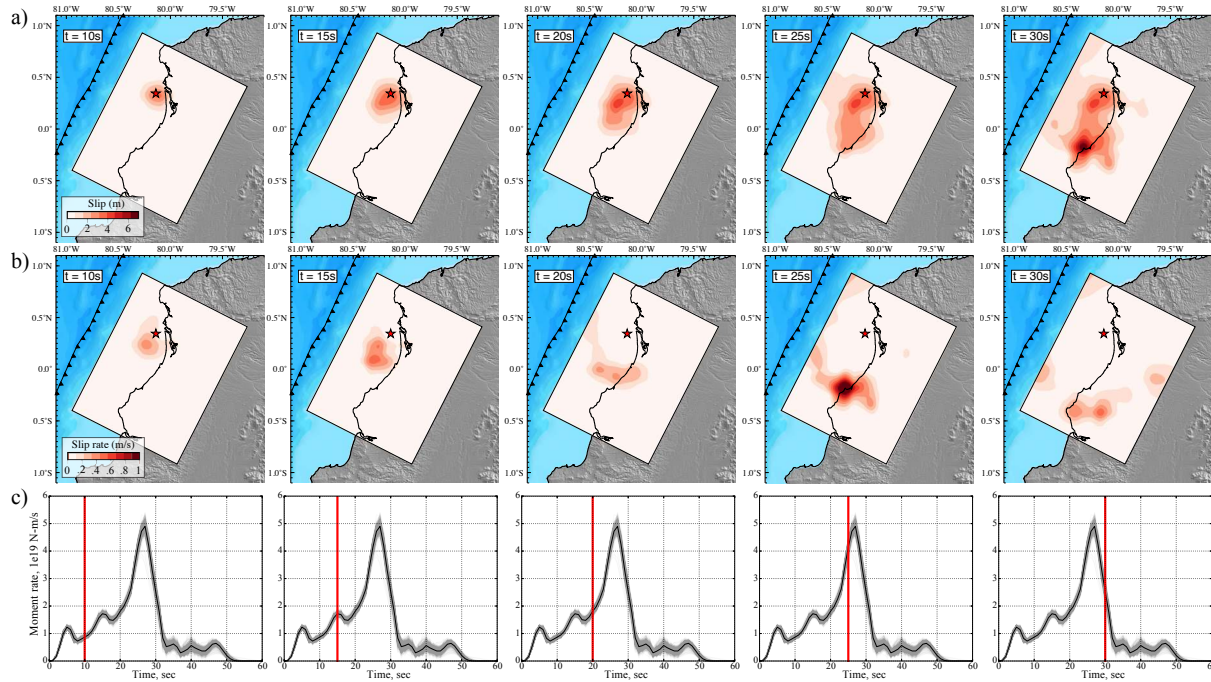


Figure 8: **Temporal evolution of co-seismic slip.** a) Cumulative slip on the fault 10 s, 15 s, 20 s, 25 s, and 30 s after the origin time. The red colour-scale indicates slip amplitude. The red star marks the epicenter location. b) Evolution of slip rate on the fault. c) Source time function (STF) of the event. Grey lines are stochastic STFs inferred from our model population while the black curve represents the posterior mean STF. Vertical red lines indicate the temporal position of each one of the snapshots

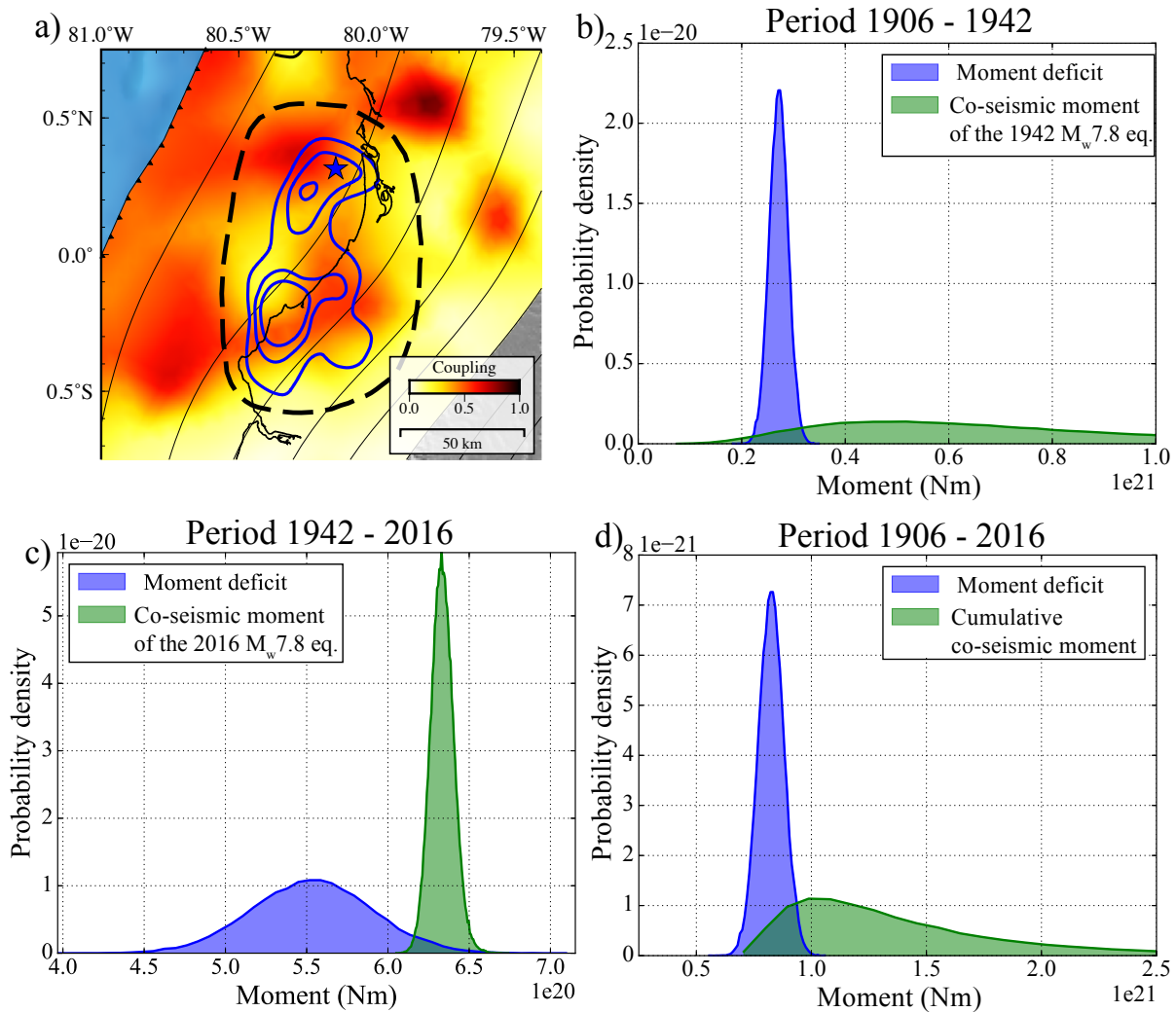


Figure 9: **Comparison of co-seismic moment and moment deficit.** a) The background colour represents the coupling posterior mean model. The blue stars shows the hypocentre location. Blue lines are the 2m, 3m, and 4m co-seismic slip isocontours. The black dashed line delimits the area where the co-seismic moment and moment deficit are computed. b) Probability densities of the co-seismic moment released by the 1942 earthquake and the moment deficit accumulated between 1906 and 1942 within the dashed ellipse shown in a). c) Probability densities of the co-seismic moment released by the 2016 earthquake and the moment deficit accumulated between 1942 and 2016. d) Probability densities of the co-seismic moment released by the sum of the 1942 and 2016 events, and of the moment deficit during the 1906 - 2016 period.

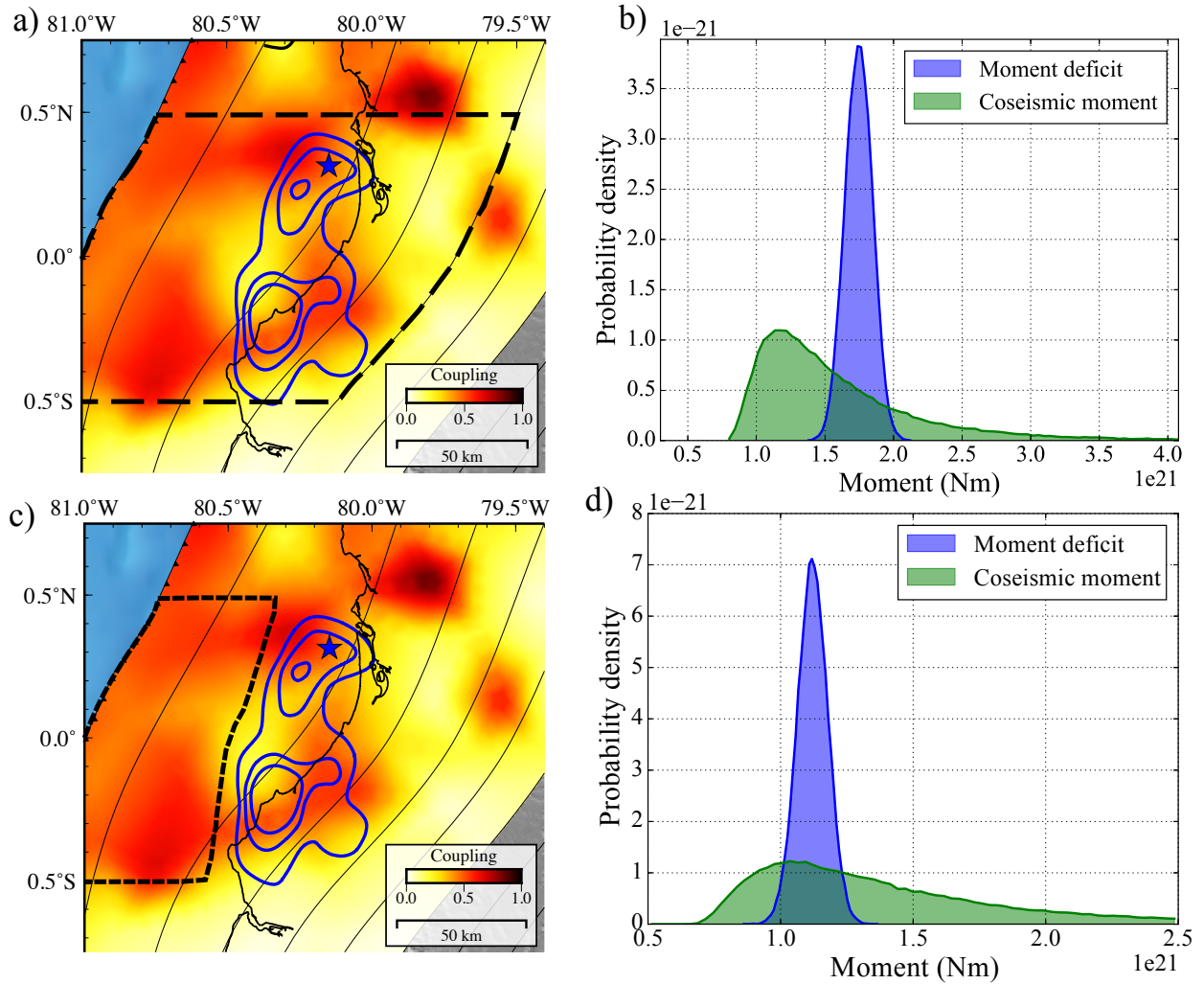


Figure 10: **Comparison of co-seismic moment and moment deficit considering the 1942 event happened at a different location.** **a)** Same as Figure 9a. The black dashed line delimits the area between 0.5°S and 0.5°N where the co-seismic moment and moment deficit are computed. **b)** Probability densities of the co-seismic moment and moment deficit in the 1906-2016 period. The co-seismic moment is the sum of the 1942 and 2016 events moment. **c)** Same as a), but the dashed black area shows where the 1942 earthquake could have been located. **d)** Probability densities of the co-seismic moment and moment deficit. The co-seismic moment is the sum of the 1942 and 2016 events moment. The moment deficit is the sum of the moment deficits computed in the updip section (shown in c)) for the 1942 - 2016 period and in the downdip section (ellipse in 9a) for the 1906 - 2016 period.

Supporting information for the main manuscript:

”Strain budget of the Ecuador-Colombia subduction zone: a stochastic view”

B. Gombert¹, Z. Duputel¹, R. Jolivet ², M. Simons³, J. Jiang⁴, C. Liang⁵, E. Fielding⁵, and L. Rivera¹

¹ Institut de Physique du Globe de Strasbourg, UMR7516, Université de Strasbourg, EOST/CNRS

² Laboratoire de géologie, Département de Géosciences, École Normale Supérieure, PSL Research University, CNRS UMR, Paris, France

³ Seismological Laboratory, Geological and Planetary Sciences, California Institute of Technology, Pasadena, California, USA

⁴ Institute of Geophysics and Planetary Physics, University of California, San Diego, La Jolla, California, USA

⁵ Jet Propulsion Laboratory, California Institute of Technology, Pasadena, California, USA

This electronic supplement is a collection of additional figures referenced in the main article. These figures were added to ensure the precision of the description of our method and results.

Supplementary text T1

Following Ye et al. (2014) and Nocquet et al. (2017), we compare waveforms of the 1942 earthquake recorded at the DBN station (De Bilt, Netherlands) with stochastic waveform predictions at the same station for the 2016 Pedernales slip distribution.

We compute displacement Green's functions for each subfault patch using the Kikuchi-Kanamori program (Kikuchi and Kanamori, 2003; Kikuchi, Masayuki and Kanamori, Hiroo, 1982). For comparison, we then convolve predicted stochastic waveforms with the instrumental response of the Galitzin seismometer that recorded the 1942 earthquake (pendulum and galvanometer periods $T_p=T_g=25$ s and gain factor $V_m=310$; Charlier and Van Gils, 1953).

In Fig. S10a, we first compare 1942 waveforms with predictions of the kinematic slip model (i.e., for the posterior distributions of slip, rise-times, rupture velocities) and hypocenter location obtained for the 2016 Pedernales earthquake. Model predictions show poor fit to the 1942 earthquake waveform. In Fig. S10b, we then compute predictions for the same kinematic slip distribution, but with a hypocenter location between the two slip asperities. With that hypocenter location, model predictions have a very good fit to the 1942 waveform. Finally, in Fig. S10c, we predict waveforms for a slip distribution on the megathrust interface, but updip of the actual 2016 rupture. Notice, that the dip is different due to the variation of the slab interface geometry with depth. We also correct the slip amplitude for the variation of shear modulus in our velocity model (cf., Fig. S2). Similarly to the previous case, the hypocenter is located between the two slip asperities. In this scenario, we are also able to explain the 1942 waveform. It illustrates that the teleseismic P-waveform is mostly sensitive to the relative location of the hypocenter and slip asperity rather than the absolute location of the earthquake.

Supplementary movie M1: Variability in the Ecuador-Colombia geodetic coupling solution The animation is made with 150 models randomly selected in the posterior population represented by the background colour. Grey lines are the 2 m contour intervals of 150 co-seismic models also randomly selected in the posterior population.

Supplementary movie M2: Temporal evolution of co-seismic slip of the 2016 Pedernales earthquake. (left) Posterior mean model of the cumulative slip. The bottom-right inset shows the stochastic source time function. **(right)** Incremental slip on the fault. The red star marks the inverted posterior mean hypocenter location.

Supplementary movie M3: Variability in the 2016 Pedernales earthquake co-seismic slip distribution solution The animation is made with 200 models randomly selected in the posterior population.

Table S1: InSAR observations used in this study.

Satellite	Orbit	Acquisition dates	N° of data	Std.	Corr. length
ALOS-2	ascending	07/02/16 - 01/05/16	130	5.3 mm	2.88 km
ALOS-2	descending	01/04/16 - 29/04/16	483	9.2 mm	11.90 km
Sentinel-1A	descending	12/04/16 - 24/04/16	380	5.0 mm	15.0 km

Table S2: Seismological data and filtering used in this study. We use a 4th order Butterworth bandpass filter.

Station	Type	Filter corner frequencies		
		East	North	Up
bahi	HRGPS	0.015Hz - 0.08Hz	0.015Hz - 0.08Hz	0.015Hz - 0.08Hz
cabp	HRPGS	0.015Hz - 0.08Hz	0.015Hz - 0.08Hz	0.015Hz - 0.08Hz
ecec	HRPGS	0.015Hz - 0.08Hz	0.015Hz - 0.08Hz	0.015Hz - 0.08Hz
fffr	HRPGS	0.015Hz - 0.08Hz	0.015Hz - 0.08Hz	0.015Hz - 0.08Hz
mlec	HRPGS	0.015Hz - 0.08Hz	0.015Hz - 0.08Hz	0.015Hz - 0.08Hz
momp	HRPGS	0.015Hz - 0.08Hz	0.015Hz - 0.08Hz	0.015Hz - 0.08Hz
onec	HRPGS	0.015Hz - 0.08Hz	0.015Hz - 0.08Hz	0.015Hz - 0.08Hz
pdns	HRPGS	0.015Hz - 0.08Hz	0.015Hz - 0.08Hz	0.015Hz - 0.08Hz
ISPT	Strong motion	N/A	0.015Hz - 0.08Hz	0.015Hz - 0.08Hz
PDNS	Strong motion	0.037Hz - 0.08Hz	0.037Hz - 0.08Hz	0.015Hz - 0.08Hz
LGCB	Strong motion	0.015Hz - 0.08Hz	0.015Hz - 0.08Hz	0.015Hz - 0.08Hz
AATC	Strong motion	0.028Hz - 0.08Hz	0.028Hz - 0.08Hz	0.032Hz - 0.08Hz
AES1	Strong motion	N/A	N/A	0.015Hz - 0.08Hz
AMNT	Strong motion	N/A	0.015Hz - 0.08Hz	0.015Hz - 0.08Hz
APED	Strong motion	0.035Hz - 0.08Hz	0.035Hz - 0.08Hz	0.035Hz - 0.08Hz
ATON	Strong motion	0.015Hz - 0.08Hz	0.015Hz - 0.08Hz	0.015Hz - 0.08Hz
AV18	Strong motion	0.015Hz - 0.08Hz	0.015Hz - 0.08Hz	0.015Hz - 0.08Hz
AV21	Strong motion	0.032Hz - 0.08Hz	0.015Hz - 0.08Hz	0.015Hz - 0.08Hz

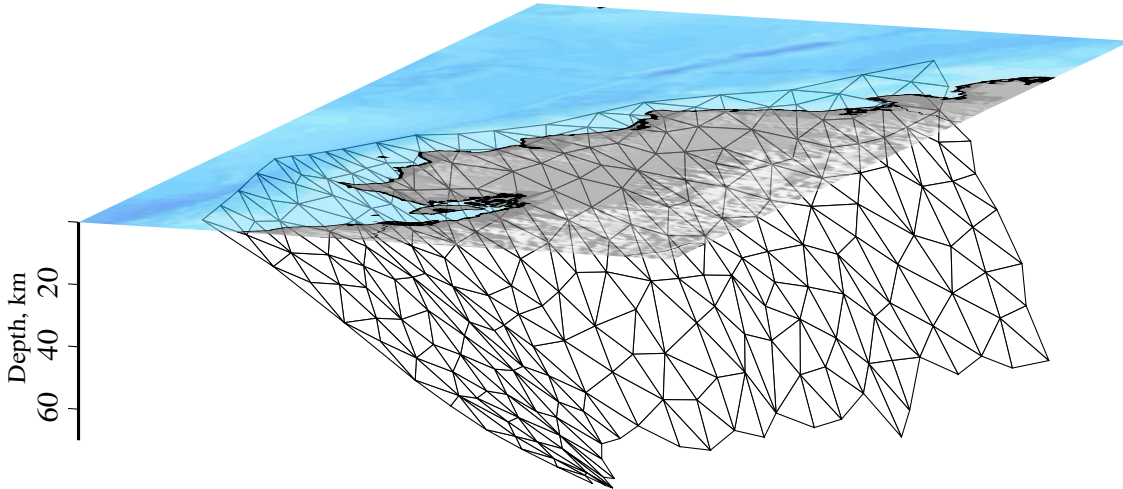


Figure S1: **Parametrization of the megathrust interface used for the coupling inversion.** Coupling value is inverted at each nodes

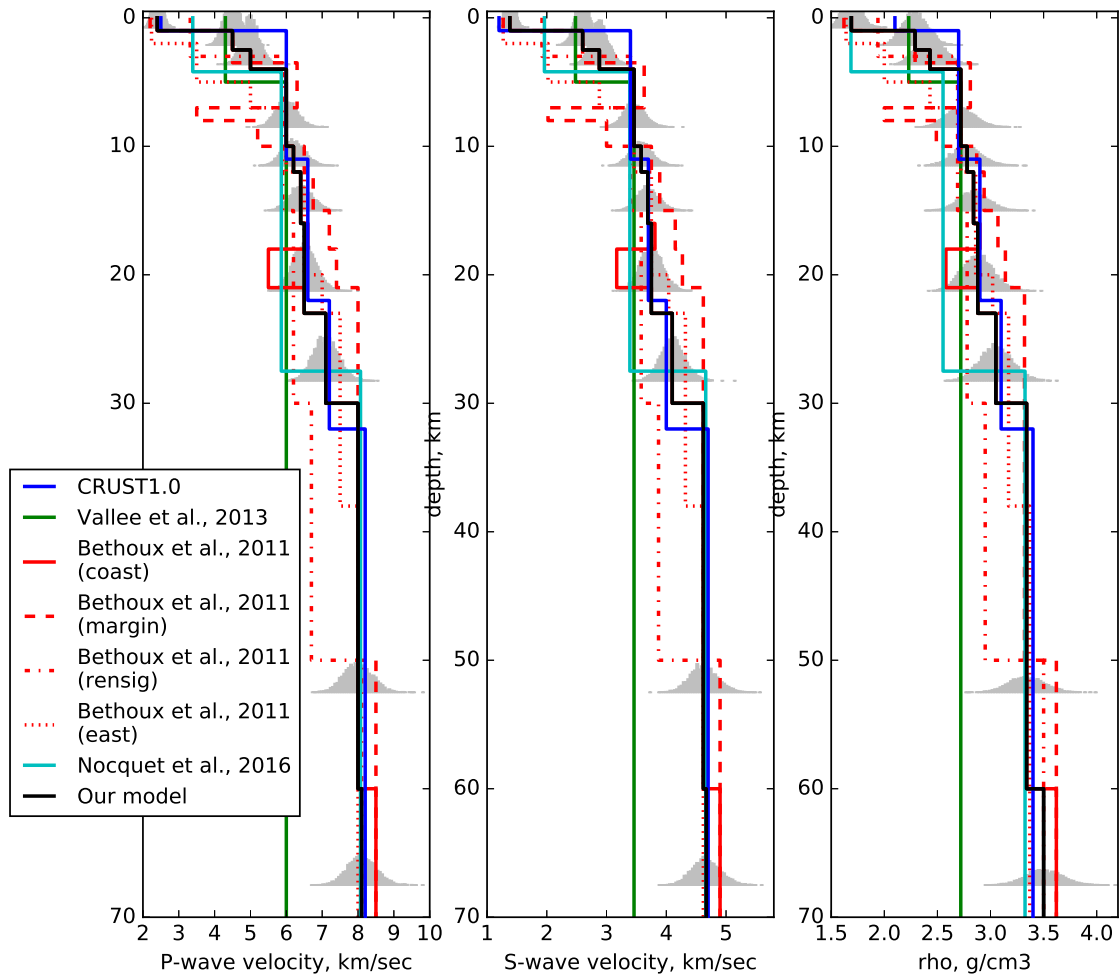


Figure S2: **Different models variability of the P-wave, S-wave, and density as a function of depth in central Ecuador.** A layered model used in this study for Green's function [GF] calculations is plotted as a solid black line. The blue line represents the CRUST2.0 model in the area (<http://igppweb.ucsd.edu/~gabi/rem.html>). The other models are from (Vallee et al., 2013; Bethoux et al., 2011; Nocquet et al., 2017). Grey histograms are the probability density function representing our confidence level on the elastic properties, as used to build the model prediction error.

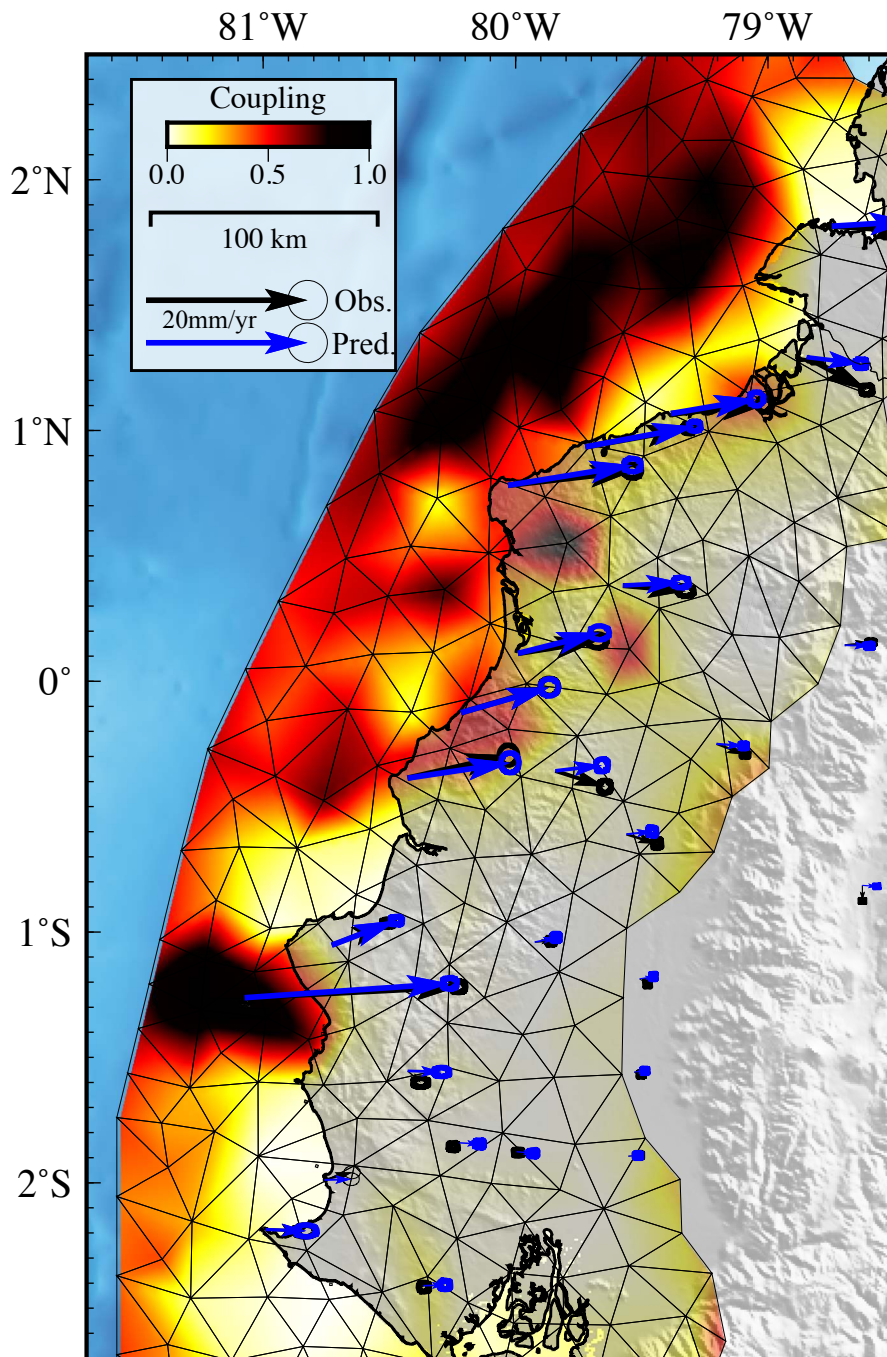


Figure S3: **Posterior Median coupling model.** Thin black lines represent the fault parametrization. Coupling values are inverted at each nodes. Interseismic GPS displacement and predictions for the median model are plotted as black and blue arrows, respectively.

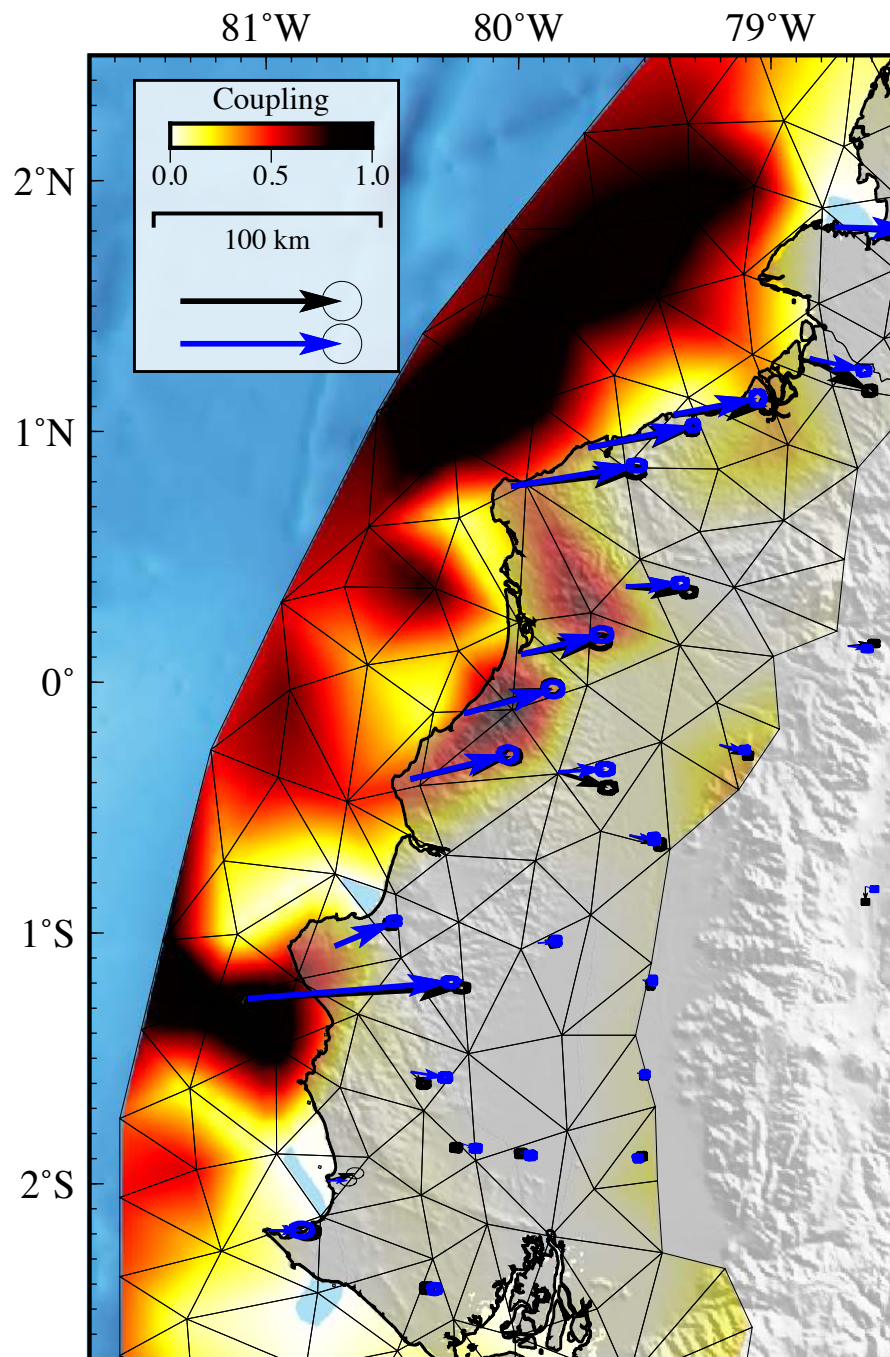


Figure S4: **Posterior Mean coupling model for a coarse parametrisation.** Same as Figure 2a. in the main text but obtained with a coarser fault parametrisation.

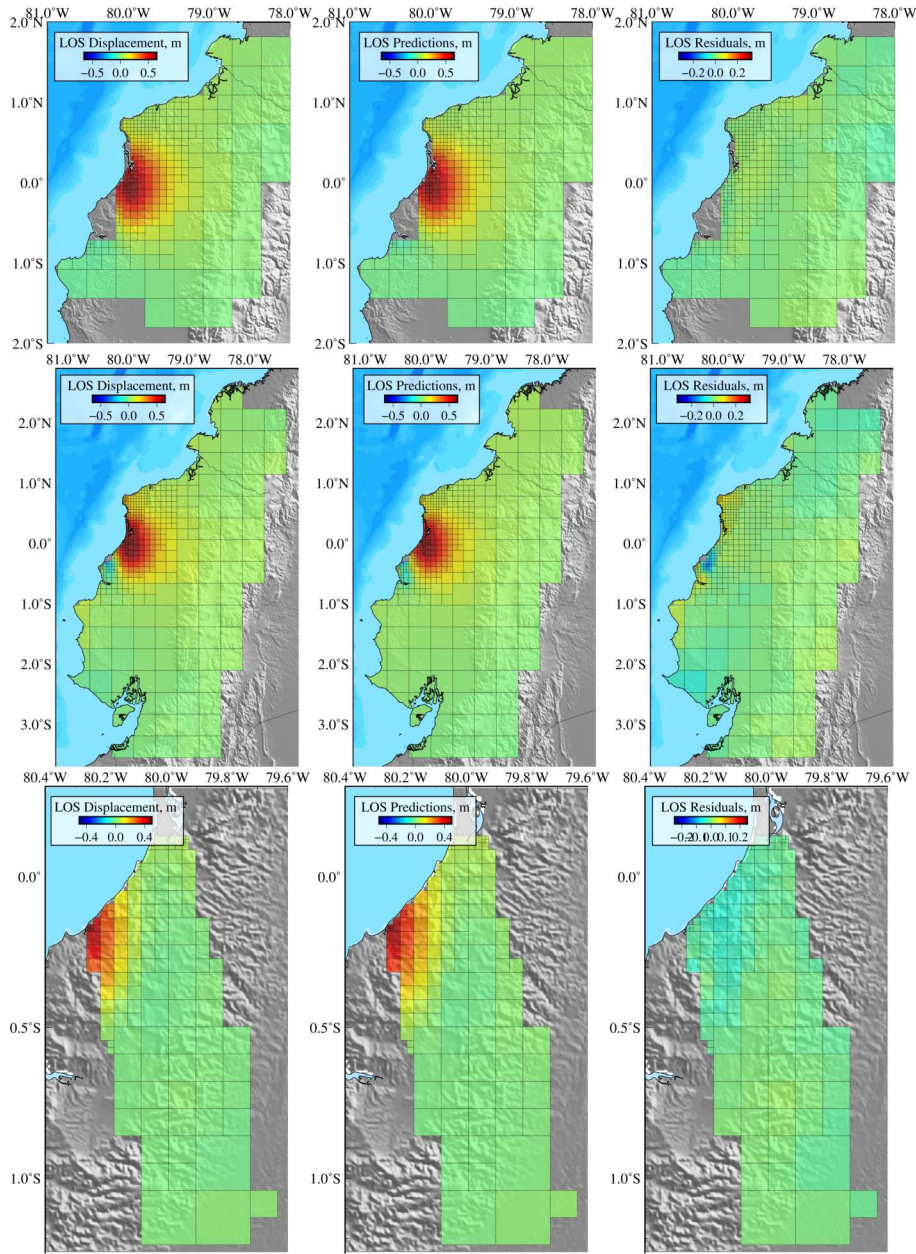


Figure S5: **Decimated InSAR observations, predictions, and residuals.** (a, d, g) Decimated InSAR observations inverted in this study. (b, e, h) Predictions for the posterior mean model. (c, f, i) Residuals of the Sentinel (top row), descending ALOS-2 (middle row), and ascending ALOS-2 (bottom row) interferograms.

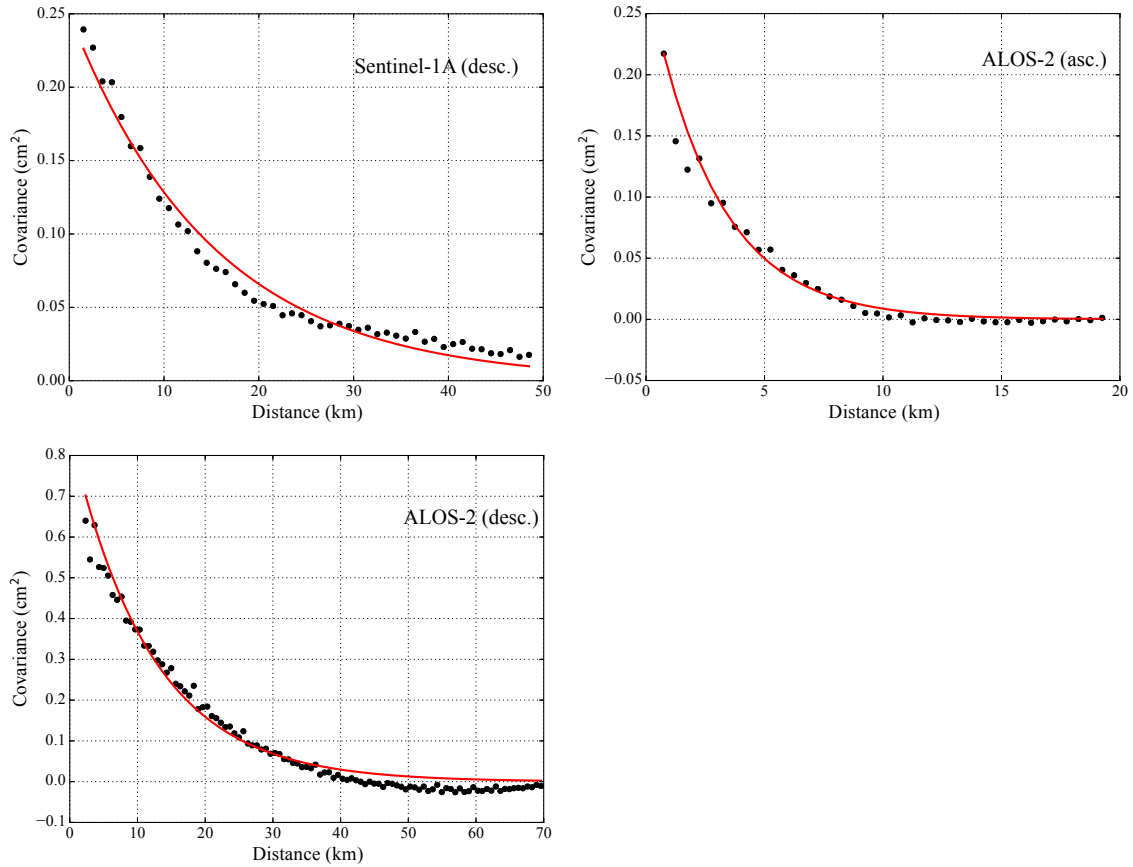


Figure S6: **Empirical covariance functions for the InSAR observations** 1D empirical covariance functions and the associated best-fit exponential function for each tracks. For each image, we compute the empirical covariance as a function of the distance between pixels and then fit an exponential function to these covariances (Jolivet et al., 2012). This exponential function is then used to build the data covariance matrix used in the inversion.

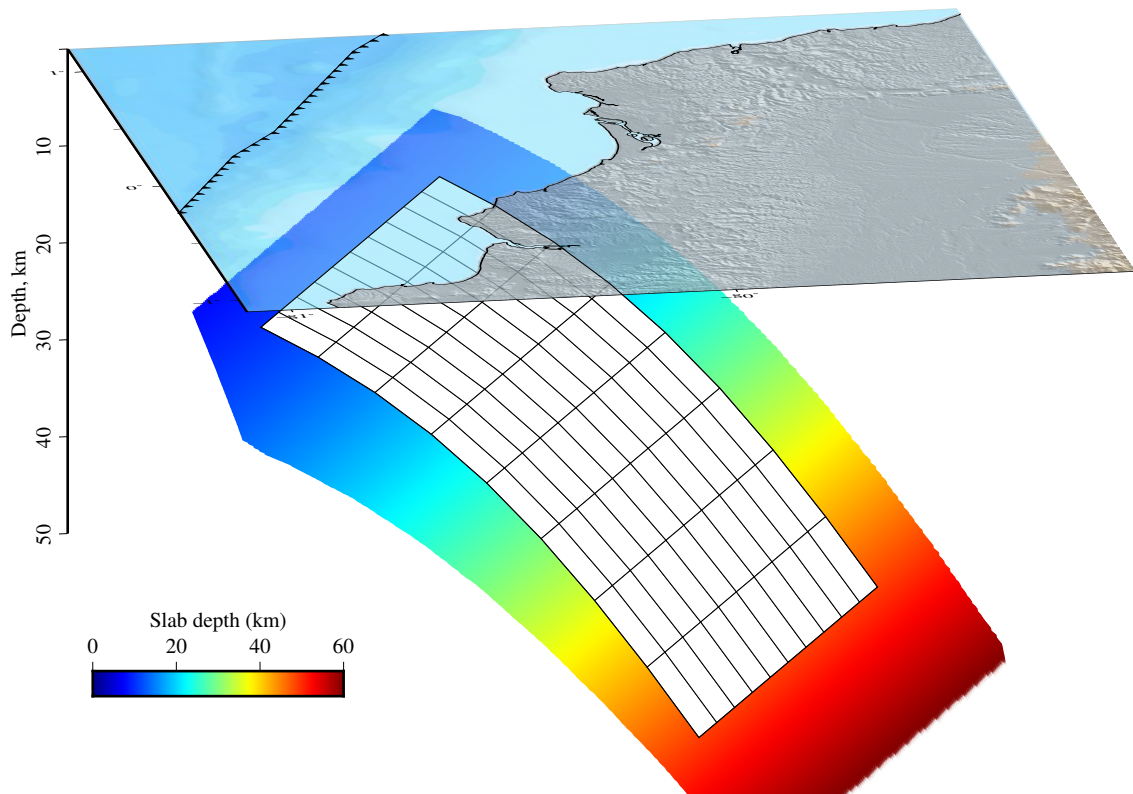


Figure S7: **Parametrization of the megathrust interface used for the co-seismic inversion**
The coloured plane represent the slab1.0 model (Hayes et al., 2012). Each subfault patch is a 15 km x 15 km square

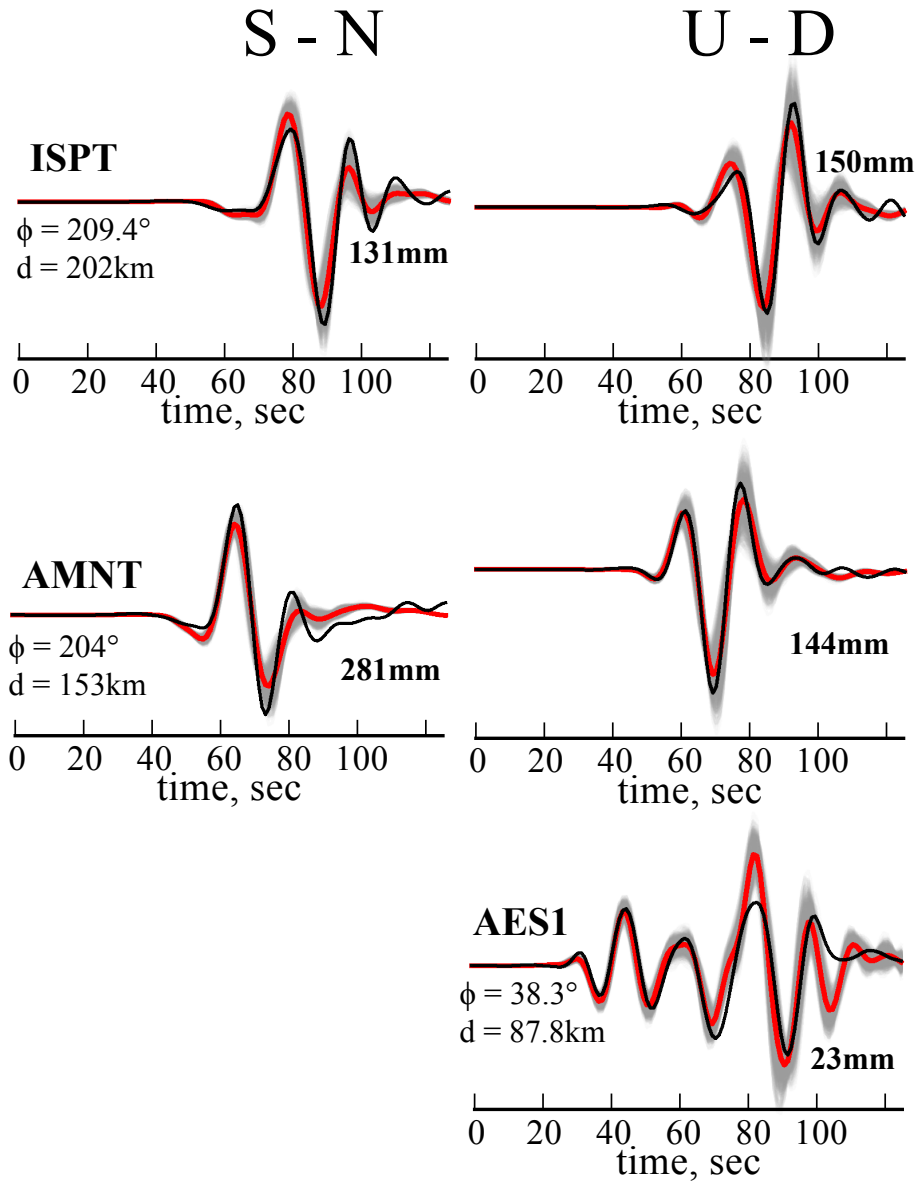


Figure S8: **Strong-motion observations and model predictions not presented in Figure 6 in the main text.** The North (left) and vertical (right) components of each station are plotted around the map. For each waveform, the bold number indicates it's maximum amplitude. The station azimuth Φ and distance d to the epicenter are also given. The black line is the recorded waveform. The gray lines are the stochastic predictions for our posterior model. The red line is the mean of the stochastic predictions.

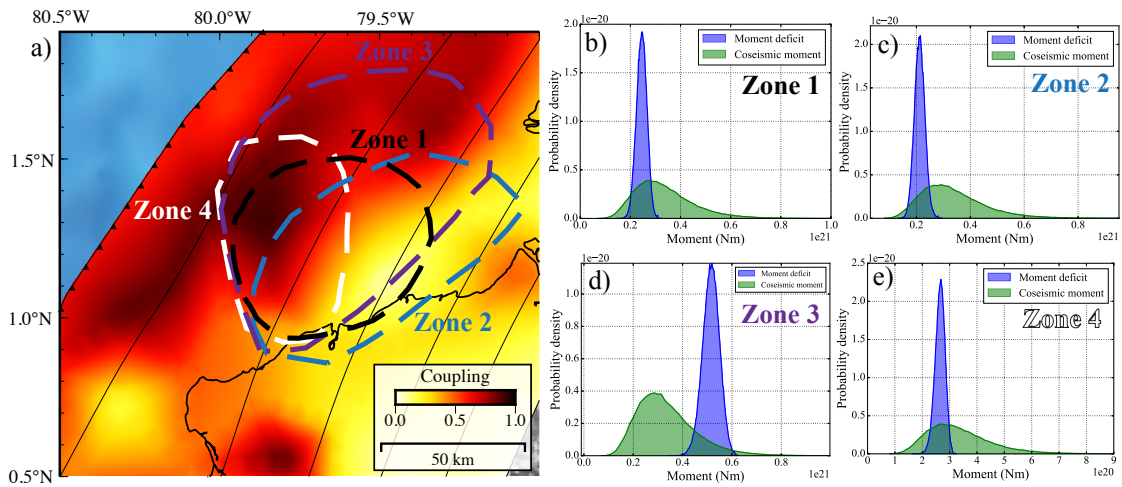


Figure S9: **Comparison of co-seismic moment and moment deficit in the 1958 earthquake region.** a) The background colour represents the coupling posterior mean model. The black dashed lines delimit four different areas where the co-seismic moment of the 1958 event and moment deficit for the 1906 - 1958 period are computed. b-e) Probability densities of the co-seismic moment released by the 1958 earthquake and the moment deficit accumulated between 1906 and 1958 in the different dashed area shown in a).

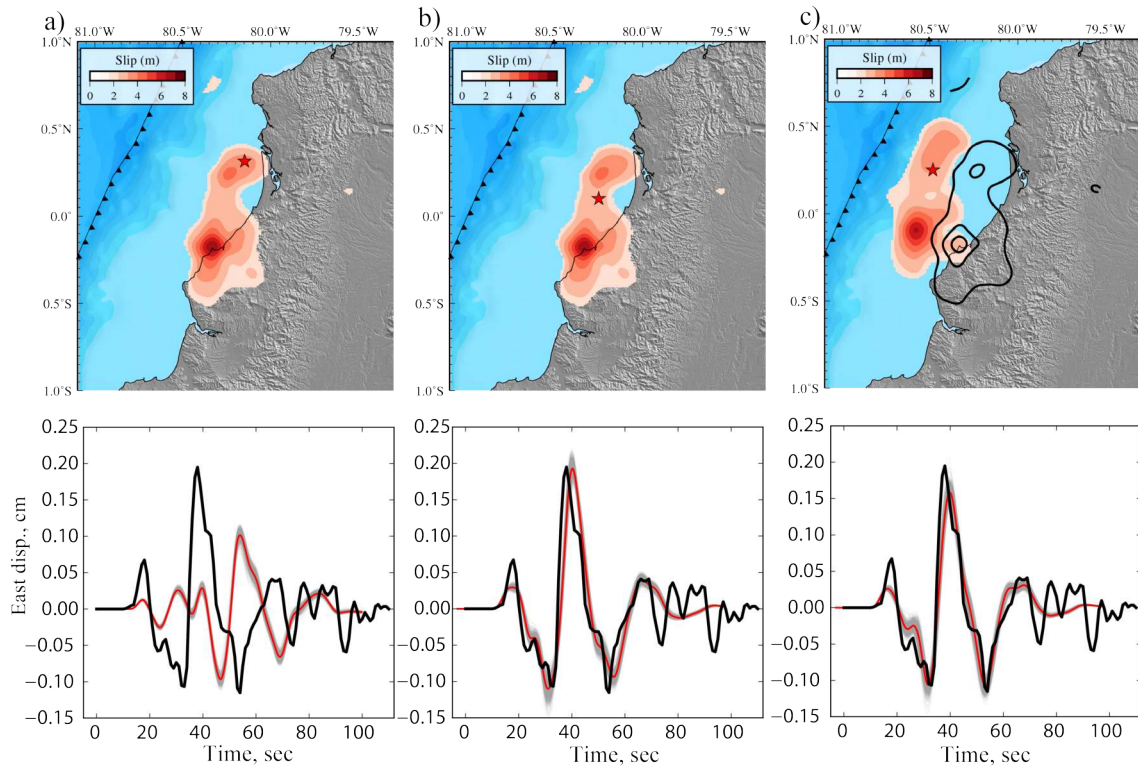


Figure S10: **Comparison of model predictions and 1942 earthquake waveform recorded in the DBN station, Netherlands.** (top) Slip model and hypocenter location (red star) used to compute the predictions shown in the bottom row. The model presented in a) results from the kinematic slip inversion of the 2016 earthquake. The models in b) and c) use a different hypocenter located between the two main slip asperities. The slip model in c) is the same as in a) and b), but located updip along the megathrust interface. Black lines in c) are slip contours of the original slip model. (bottom) East component waveform recorded at DBN for the 1942 earthquake (in black) and stochastic predictions (in grey) for the model shown on top. The red line is the posterior mean prediction. Predictions were convolved with the instrumental response of the Galitzin that recorded the event.

References

- Bethoux, N., Segovia, M., Alvarez, V., Collot, J.-Y., Charvis, P., Gailler, A., and Monfret, T. (2011). Seismological study of the central Ecuadorian margin: Evidence of upper plate deformation. *Journal of South American Earth Sciences*, 31(1):139–152.
- Charlier, C. and Van Gils, J. (1953). Liste des stations seismologiques mondiales. *Association internationale de seismologie, Observatoire Royal de Belgique*.
- Hayes, G. P., Wald, D. J., and Johnson, R. L. (2012). Slab1. 0: A three-dimensional model of global subduction zone geometries. *Journal of Geophysical Research: Solid Earth*, 117(B1).
- Jolivet, R., Lasserre, C., Doin, M.-P., Guillaso, S., Peltzer, G., Dailu, R., Sun, J., Shen, Z.-K., and Xu, X. (2012). Shallow creep on the Haiyuan fault (Gansu, China) revealed by SAR interferometry. *Journal of Geophysical Research: Solid Earth*, 117(B6).
- Kikuchi, M. and Kanamori, H. (2003). *Note on Teleseismic Body-Wave Inversion Program*. <http://www.eri.u-tokyo.ac.jp/ETAL/KIKUCHI/>.
- Kikuchi, Masayuki and Kanamori, Hiroo (1982). Inversion of complex body waves. *Bulletin of the Seismological Society of America*, 72(2):491–506.
- Nocquet, J.-M., Jarrin, P., Vallée, M., Mothes, P., Grandin, R., Rolandone, F., Delouis, B., Yepes, H., Font, Y., Fuentes, D., et al. (2017). Supercycle at the Ecuadorian subduction zone revealed after the 2016 Pedernales earthquake. *Nature Geoscience*, 10(2):145–149.
- Vallee, M., Nocquet, J.-M., Battaglia, J., Font, Y., Segovia, M., Regnier, M., Mothes, P., Jarrin, P., Cisneros, D., Vaca, S., et al. (2013). Intense interface seismicity triggered by a shallow slow slip event in the Central Ecuador subduction zone. *Journal of Geophysical Research: Solid Earth*, 118(6):2965–2981.
- Ye, L., Lay, T., Koper, K. D., Smalley Jr., R., Rivera, L., Bevis, M. G., Zakrajsek, A. F., and Teferle, F. N. (2014). Complementary slip distributions of the August 4, 2003 Mw 7.6 and November 17, 2013 Mw 7.8 South Scotia Ridge earthquakes. *Earth Planet. Sci. Lett.*, 401:215–226.